Supporting Information for "MMA-EoS: A Computational Framework for Mineralogical Thermodynamics"

T. C. Chust[1,2], G. Steinle-Neumann[1], D. Dolejš[3], B. S. A. Schuberth[2], and H.-P. Bunge[2]

Contents of this file

Introduction

The supporting online material contains the following information:

- A Section with details on the thermodynamic models for the equations-of-state used, the solution model implemented in the MMA-EoS software package, as well as details on the mixing properties in phase aggregates.
- A Section on code implementation of MMA-EoS.
- Further application of thermodynamic models:

  – Computation and comparison of Gibbs energy of the Mg_2SiO_4 and Fe_2SiO_4 polymorphs between the thermodynamic parametrizations of *Stixrude and Lithgow-Bertelloni* [2011] and *Holland et al.* [2013] (Figure S4).

  – Configurational properties for the diopside-Ca-tschermak solid solution computed with the thermodynamic database of *Stixrude and Lithgow-Bertelloni* [2011] and a comparison to calorimetric estimates (Figure S5).

  – A P-x phase diagram of the $Mg_2Si_2O_6$-$CaMgSi_2O_6$ binary ($T = 1923\,\mathrm{K}$) (Figure S6).

  – A comparison of elastic properties of garnets along the pyrope-almandine, pyrope-grossular and pyrope-majorite binaries computed with the thermodynamic database of *Stixrude and Lithgow-Bertelloni* [2011] and experimental results (Figure S7).

- Additional full P-T phase diagrams for the reduced pyrolite compositions FMS (Figure S8), CFMS (Figure S9) and CFMAS (Figure S10), as well as for the depleted mantle (Figure S11) and bulk oceanic crust (Figure S12) composition (Table 2).
- A comparison of phase diagrams for two different compositions of mid ocean ridge basalt using two different thermodynamic databases [*Xu et al.*, 2008; *Stixrude and Lithgow-Bertelloni*, 2011] (Figure S13).
- A supporting Figure, showing computed adiabatic gradients through the Earth's mantle (Figure S14).

[1]Bayerisches Geoinstitut, Universität Bayreuth, 95440 Bayreuth, Germany
[2]Department of Earth and Evironmental Sciences, Geophysics Section, Ludwig-Maximilians-Universität München, Theresienstraße 41, 80333 München, Germany
[3]Institute of Earth and Evironmental Sciences, Albert-Ludwigs-Universität Freiburg, Albertstraße 23b, 79104 Freiburg, Germany

0148-0227/17/$9.00

S1. Details of Thermodynamic Models

The MMA-EoS software contains implementations of three alternative thermodynamic models and equations-of-state to calculate Gibbs energy of condensed phases at elevated P and T: A Caloric–Murnaghan model [e.g., *Holland and Powell*, 1998; *Fabrichnaya et al.*, 2004] and a Caloric–Modified-Tait model [e.g., *Holland et al.*, 2013], both of which first follow an isobaric heating and then a thermal compression path, and a Birch-Murnaghan–Mie-Grüneisen-Debye model [e.g., *Ita and Stixrude*, 1992; *Stixrude and Lithgow-Bertelloni*, 2005, 2011], which first follows an isothermal compression and then an isochoric heating path (Figure 1).

S1.1. The Caloric–Murnaghan Model

The model follows a P-T path from the reference conditions that combines isobaric heating at reference P, formulated using an empirical heat capacity approximation, and high-T compression, based on the Murnaghan equation-of-state [*Murnaghan*, 1944] (Figure 1). This approach has been applied by *Holland and Powell* [1998], *Matas* [1999], *Fabrichnaya et al.* [2004] and *Piazzoni et al.* [2007]. The dataflow is illustrated in Figure S1.

The molar Gibbs energy of a phase at P and T of interest consists of the following contributions:

$$\begin{aligned} G(P,T) = {} & H_0 + [H(P_0,T)]_{T_0}^{T} \\ & - T\left(S_0 + [S(P_0,T)]_{T_0}^{T}\right) \\ & + [G(P,T)]_{P_0}^{P}, \end{aligned} \tag{S1}$$

where subscript 0 indicates a quantity at reference conditions (P_0, T_0). The molar caloric enthalpy $H(P_0,T)$ and the entropy contribution at reference pressure $S(P_0,T)$ are evaluated using the isobaric heat capacity C_P:

$$[H(P_0,T)]_{T_0}^{T} = \int_{T_0}^{T} C_P(T)\,\mathrm{d}T, \tag{S2}$$

and

$$[S(P_0,T)]_{T_0}^{T} = \int_{T_0}^{T} \frac{C_P(T)}{T}\,\mathrm{d}T, \tag{S3}$$

where

$$C_P(T) = \sum_i c_i T^{p_i}. \tag{S4}$$

The number and values of coefficients and exponents in Equation (S4) are generally variable and chosen empirically [*Holland and Powell*, 1998; *Bale et al.*, 2002; *Fabrichnaya et al.*, 2004]. The implementation in MMA-EoS allows for the specification of arbitrary polynomials, which are differentiated and integrated analytically. For instance, *Fabrichnaya et al.* [2004] and *Holland and Powell* [1998, 2011] use seven and four parameters, respectively, with positive and negative integer and rational exponents.

The contribution to G from compression at elevated T is computed as the volume-work integral

$$[G(P,T)]_{P_0}^{P} = \int_{P_0}^{P} V(P,T)\,\mathrm{d}P, \tag{S5}$$

with molar volume V. In the model of *Fabrichnaya et al.* [2004], it is described by the second-order Murnaghan equation-of-state:

$$V(P,T) = V(P_0,T)\left(1 + \frac{\partial_P K(T) P}{K(T)}\right)^{-\frac{1}{\partial_P K(T)}}, \tag{S6}$$

where K is the isothermal bulk modulus and $\partial_P K$ its pressure derivative. Throughout the presentation of models, we use the notation ∂_X to denote a partial derivative with respect to X and we apply the convention that differential operators take precedence over the reference state indicator, i.e., $\partial_{P,T} K_0 = (\partial_P \partial_T K)(P_0, T_0)$ represents the P-T-cross derivative of the isothermal bulk modulus, evaluated at the reference point (P_0, T_0).

The volume and bulk modulus of the phase at reference pressure and elevated temperature are frequently evaluated by semi-empirical functions. For the T-dependence of volume and the thermal expansivity α, MMA-EoS uses

$$V(P_0,T) = V_0 e^{\int_{T_0}^{T} \alpha(T)\,dT}, \tag{S7}$$

$$\alpha(T) = \sum_j a_j T^{p_j}, \tag{S8}$$

which is, e.g., compatible with the formulation by *Fabrichnaya et al.* [2004]:

$$\alpha(T) = a_1 + a_2 T + a_3 T^{-1} + a_4 T^{-2}. \tag{S9}$$

The isothermal bulk modulus K of the phase is described as a linear or polynomial function of T. In this case, the formulation in MMA-EoS accounts for the direct T-dependence of K and $\partial_P K$ and an implicit entropy dependence of $\partial_P K$ [*Poirier*, 2000]:

$$K(T) = K_0 + \partial_T K_0 (T - T_0), \tag{S10}$$

$$\partial_P K(T) = \partial_P K_0 + \partial_{P,T} K_0 (T - T_0)(\ln T - \ln T_0), \tag{S11}$$

which is, e.g., compatible with the parameterization used by *Piazzoni et al.* [2007] or *Matas* [1999].

Alternatively, K at P_0 is expressed in terms of isothermal compressibility β:

$$K(T) = \frac{1}{\beta(T)}, \tag{S12}$$

$$\beta(T) = \sum_k b_k T^{p_k}, \tag{S13}$$

which is, in turn, compatible with the parameterization used by *Fabrichnaya et al.* [2004].

While the polynomial approximations of C_P and K can produce very accurate results in the T-range of calibration, they extrapolate poorly and their functional form does not guarantee physically sensible behavior under extreme conditions.

Any other thermodynamic equilibrium property of a particular phase is obtained by differentiating the leading potential function and using standard thermodynamic identities. Entropy of a phase, for example, is calculated as follows:

$$S(P,T) = -\partial_T G(P,T) \tag{S14}$$

$$\begin{aligned} & = S(P_0,T) + T\partial_T S(P_0,T) \\ & \quad - \partial_T [H(P_0,T)]_{T_0}^{T} - \partial_T [G(P,T)]_{P_0}^{P} \\ & = S(P_0,T) + T\partial_T S(P_0,T) - C_P(T) \\ & \quad - \int_{P_0}^{P} \partial_T V(P,T)\,\mathrm{d}P \\ & = S_0 + \int_{T_0}^{T} \frac{C_P(T)}{T}\,\mathrm{d}T - \int_{P_0}^{P} \alpha(T) V(P,T)\,\mathrm{d}P. \end{aligned} \tag{S15}$$

Density can be computed directly through its relationship to V:

$$\rho(P,T) = \frac{M}{V(P,T)}, \tag{S16}$$

where M is the molar mass of the phase of interest.

The compressibility can (also) be expressed as

$$\beta(P,T) = -\frac{1}{V(P,T)}\partial_P V(P,T) = (K(T) + \partial_P K(T) P)^{-1} \tag{S17}$$

for the second order equation-of-state introduced in Equation (S6).

S1.2. The Caloric–Modified-Tait Model

This model is conceptually similar to the Caloric–Murnaghan model, but employs a different P-V equation-of-state [*Holland and Powell*, 2011; *Holland et al.*, 2013]. For an overview of the dataflow see Figure S1.

In analogy to the Caloric–Murnaghan model, Gibbs energy is computed by T-integration over C_P at P_0 and P-integration over V at elevated T to obtain Gibbs energy (Equations (S1), (S2) and (S5)). To obtain $V(P,T)$, the modified Tait equation is used in *Holland and Powell* [2011]:

$$V(P,T) = V_0(1 - a(1 - (1 + b(P - P_{\mathrm{th}}(T)))^{-c})), \tag{S18}$$

where P_{th} is thermal pressure and a, b, c depend on compressibility parameters:

$$a = \frac{1 + \partial_P K_0}{1 + \partial_P K_0 + K_0 \partial_P^2 K_0}, \tag{S19}$$

$$b = \frac{\partial_P K_0}{K_0} - \frac{\partial_P^2 K_0}{1 + \partial_P K_0}, \tag{S20}$$

$$c = \frac{1 + \partial_P K_0 + K_0 \partial_P^2 K_0}{\partial_P K_0^2 + \partial_P K_0 - K_0 \partial_P^2 K_0}. \tag{S21}$$

Substituting Equation (S18) into (S5) yields

$$[G(P,T)]_{P_0}^{P} = P V_0 \left(1 - a + a\frac{(1 - bP_{\mathrm{th}}(T))^{1-c}}{b(c-1)P} - \frac{(1 + b(P - P_{\mathrm{th}}(T)))^{1-c}}{b(c-1)P}\right). \tag{S22}$$

The thermal pressure used by *Holland and Powell* [2011] is inspired by the Einstein lattice vibration model and includes an approximate Einstein temperature θ_{E}:

$$P_{\mathrm{th}}(T) = \alpha_0 K_0 \frac{\theta_{\mathrm{E}}}{\xi(T_0)}\left(\frac{1}{e^{\frac{\theta_{\mathrm{E}}}{T}} - 1} - \frac{1}{e^{\frac{\theta_{\mathrm{E}}}{T_0}} - 1}\right), \tag{S23}$$

with

$$\xi(T) = \frac{\left(\frac{\theta_{\mathrm{E}}}{T}\right)^2 e^{\frac{\theta_{\mathrm{E}}}{T}}}{(e^{\frac{\theta_{\mathrm{E}}}{T}} - 1)^2}, \tag{S24}$$

$$\theta_{\mathrm{E}} = \frac{10636.0\,\mathrm{K}}{\frac{S_0}{N\mathrm{Jmol^{-1}K^{-1}}} + 6.44}. \tag{S25}$$

The Einstein temperature θ_{E} depends on the entropy of the reference state S_0 and the number of atoms per formula unit N.

By differentiating $V(P,T)$ (Equation (S18)) we obtain α and β of a phase:

$$\alpha(P,T) = \frac{\alpha_0 K_0 \theta_{\mathrm{E}}}{\xi(T_0)} \cdot \frac{abc(1 + b(P - P_{\mathrm{th}}(T)))^{-c-1} e^{\frac{\theta_{\mathrm{E}}}{T}} \frac{\theta_{\mathrm{E}}}{T^2}}{(1 - a(1 - (1 + b(P - P_{\mathrm{th}}(T)))^{-c}))(e^{\frac{\theta_{\mathrm{E}}}{T}} - 1)^2}, \tag{S26}$$

$$\beta(P,T) = \frac{1}{K_0} \cdot (1 + b(P - P_{\mathrm{th}}))^{-1} \cdot (a + (1 - a)(1 + b(P - P_{\mathrm{th}}))^{c})^{-1}. \tag{S27}$$

Any other thermodynamic property is obtained by differentiation of the Gibbs potential at P, T and by applying thermodynamic identities as illustrated in Equation (S15) for entropy.

S1.3. The Birch-Murnaghan–Mie-Grüneisen-Debye Model

Here, the thermodynamic potential is computed along an integration path that combines isothermal compression at T_0 up to the elastic pressure P_{el} and isochoric heating to the P and T of interest (Figure 1). The model formulation follows *Stixrude and Lithgow-Bertelloni* [2005, 2011] and is compatible with datasets in these publications. For an overview of the dataflow see Figure S1.

The expression for Gibbs energy of a phase at elevated P and T consists of individual contributions to Helmholtz energy A and a conversion term accounting for the change of conditions from constant-V to constant-P:

$$G(P,T) = A_0 - [A(f,T_0)]_{f(V_0)}^{f(V)} - [A(f_1,T)]_{T_0}^{T} + P\,V(P,T), \qquad (f_1 = f(P,T)). \tag{S28}$$

The Birch-Murnaghan equation-of-state [*Birch*, 1947] is applied to expand P_{el} and V as polynomials in the finite strain parameter f:

$$f(V) = \frac{1}{2}\left(\left(\frac{V}{V_0}\right)^{-\frac{2}{3}} - 1\right) \iff V(f) = V_0(2f+1)^{-\frac{3}{2}}, \tag{S29}$$

$$P(f,T) = P_{\mathrm{el}}(f) + P_{\mathrm{th}}(f,T), \tag{S30}$$

$$P_{\mathrm{el}}(f) = 3K_0(2f+1)^{\frac{5}{2}}\left(f + \frac{3}{2}(\partial_P K_0 - 4)f^2\right). \tag{S31}$$

To obtain $f(P,T)$ and consequently $V(f(P,T))$, the model implementation in MMA-EoS inverts Equation (S30) numerically for f at constant T. Once f is determined, the isothermal contribution to Helmholtz energy can be computed as

$$[A(f,T_0)]_{f(V_0)}^{f(V)} = \int_{V_0}^{V(f)} P(f(V),T_0)\,\mathrm{d}V \tag{S32}$$

$$= \int_{f(V_0)}^{f} P_{\mathrm{el}}(f)\partial_f V(f)\,\mathrm{d}f \tag{S33}$$

$$= -\frac{9}{2}K_0 V_0\left(f^2 + (\partial_P K_0 - 4)f^3\right). \tag{S34}$$

Thermal effects, on the other hand, are computed from a lattice vibration model based on *Debye* [1912], from which expressions for the thermal contribution to Helmholtz energy $[A(f,T)]_{T_0}^{T}$, thermal pressure P_{th} and entropy S can be derived [*Poirier*, 2000]. These can be transformed from constant-V to constant-P conditions [*Ita and Stixrude*, 1992; *Stixrude and Lithgow-Bertelloni*, 2005, 2011]:

$$\begin{aligned}[A(f,T)]_{T_0}^{T} &= \int_{T_0}^{T} S(V(f),T)\,\mathrm{d}T \qquad \text{(S35)}\\ &= -NR\Big[T\Big(3\ln\Big(1-e^{-x(f,T)}\Big)\\ &\quad+\frac{9}{8}x(f,T) - D_3(x(f,T))\Big)\Big]_{T_0}^{T}, \qquad \text{(S36)}\end{aligned}$$

and

$$\begin{aligned}P_{\mathrm{th}}(f,T) &= 3NR\,[TD_3(x(f,T))]_{T_0}^{T}\,\frac{\gamma(f)}{V(f)}, \qquad \text{(S37)}\\ S(P,T) &= 4NRD_3(x(f(P,T),T))\\ &\quad-3NR\ln\Big(1-e^{-x(f(P,T),T)}\Big)\\ &\quad+\int_0^T V(P,T)\frac{\alpha(P,T)^2}{\beta(P,T)}\,\mathrm{d}T, \qquad \text{(S38)}\end{aligned}$$

with

$$\begin{aligned}\theta_{\mathrm{D}}(f) &= \theta_{D,0}\sqrt{1+6\gamma_0 f+\frac{1}{2}g_0 f^2}, \qquad \text{(S39)}\\ x(f,T) &= \frac{\theta_{\mathrm{D}}(f)}{T}, \qquad \text{(S40)}\\ \gamma(f) &= \frac{(6\gamma_0+g_0 f)(2f+1)}{6+36\gamma_0 f+3g_0 f^2}, \qquad \text{(S41)}\\ g_0 &= 36\gamma_0^2-12\gamma_0-18q_0\gamma_0, \qquad \text{(S42)}\end{aligned}$$

where θ_{D} is the Debye temperature and γ the Grüneisen parameter.

The integral in Equation (S35) is replaced using the third-order Debye function, which appears in Equations (S36) – (S38):

$$D_3(x) = \frac{3}{x^3}\int_0^x \frac{t^3}{e^t-1}\,\mathrm{d}t. \qquad \text{(S43)}$$

For the numerical approximation used to evaluate the Debye integral in (S43) see Section S2.3.

Similarly, C_P can be computed from S by differentiating Equation (S38):

$$\begin{aligned}C_P(P,T) &= T\partial_T S(P,T) \qquad \text{(S44)}\\ &= C_V(f(P,T),T) + V(P,T)T\frac{\alpha(P,T)^2}{\beta(P,T)}\\ &= 3NR\left(4D_3(x(f(P,T),T)) - \frac{3x(f(P,T),T)}{e^{x(f(P,T),T)}-1}\right)\\ &\quad+V(P,T)T\frac{\alpha(P,T)^2}{\beta(P,T)}. \qquad \text{(S45)}\end{aligned}$$

For the isochoric heat capacity C_V (first term in Equation S45), the model shows the following behavior in the high-T limit:

$$\begin{aligned}\lim_{T\to\infty} x(f(P,T),T) &= 0, \qquad \text{(S46)}\\ \lim_{x\to 0} D_3(x) &= 1, \qquad \text{(S47)}\\ e^x - 1 &\approx x \qquad (x \ll 1) \qquad \text{(S48)}\\ \implies \lim_{T\to\infty} C_V(P,T) &= 3NR, \qquad \text{(S49)}\end{aligned}$$

consistent with the law of Dulong-Petit. As T approaches zero one obtains

$$\begin{aligned}\lim_{T\to 0} x(f(P,T),T) &= \infty, \qquad \text{(S50)}\\ \lim_{x\to\infty} D_3(x) &= 0 \qquad \text{(S51)}\\ \implies \lim_{T\to 0} C_V(P,T) &= 0, \qquad \text{(S52)}\end{aligned}$$

in agreement with the third law of thermodynamics. The high- and low-T limits guarantee that the model behaves in a physically sensible way at any T, even when extrapolating beyond the conditions for which model parameters have originally been fitted.

Derivative volumetric properties can be computed using standard thermodynamic relationships:

$$\begin{aligned}\alpha(P,T) &= \frac{1}{V(P,T)}\partial_T V(P,T), \qquad \text{(S53)}\\ \beta(P,T) &= -\frac{1}{V(P,T)}\partial_P V(P,T). \qquad \text{(S54)}\end{aligned}$$

Finally, the adiabatic bulk modulus κ can be derived from the Gibbs potential:

$$\begin{aligned}\kappa(f,T) &= \frac{\partial_P G}{\frac{(\partial_{T,P}G)^2}{\partial_T^2 G} - \partial_P^2 G} \qquad \text{(S55)}\\ &= (2f+1)^{5/2}K_0\\ &\quad\cdot\left(1+\left((3\partial_P K_0-5)f+\frac{27}{2}(\partial_P K_0-4)f^2\right)\right)\\ &\quad+\frac{\gamma(f)(\gamma(f)+1-q(f))}{V(f)}[E(f,T)]_{T_0}^{T}\\ &\quad-\frac{\gamma(f)^2}{V(f)}[TC_V(f,T)]_{T_0}^{T}, \qquad \text{(S56)}\end{aligned}$$

with

$$\begin{aligned}[E(f,T)]_{T_0}^{T} &= 3NR[TD_3(x)]_{T_0}^{T}, \qquad \text{(S57)}\\ q(f) &= 2\left(\gamma(f)-\frac{1}{3}\right) - \frac{g_0(2f+1)}{3(6\gamma_0+g_0 f)}, \qquad \text{(S58)}\end{aligned}$$

where $[E(f,T)]_{T_0}^{T}$ represents the thermal internal energy derived from the Debye model [*Ashcroft and Mermin*, 1976].

S1.4. Shear Modulus

A shear modulus μ can be formulated consistently with the Birch-Murnaghan–Mie-Grüneisen-Debye model [*Stixrude and Lithgow-Bertelloni*, 2005], although the thermodynamic theory of the model does not provide information about shear deformation directly, as it accounts for isotropic deformation only. The computation of μ requires some additional model parameters:

$$\begin{aligned}\mu(f,T) &= (2f+1)^{5/2}\mu_0\\ &\quad+(2f+1)^{5/2}f(3K_0\mu_{P,0}-5\mu_0)\\ &\quad+(2f+1)^{5/2}f^2\\ &\quad\cdot\left(6K_0\mu_{P,0}-24K_0-14\mu_0+\frac{9}{2}K_0\partial_P K_0\right)\\ &\quad-\eta_S\frac{[E(f,T)]_{T_0}^{T}}{V(f)}. \qquad \text{(S59)}\end{aligned}$$

The shear modulus at reference condition is μ_0 and its pressure derivative $\mu_{P,0}$. The shear strain derivative η_S of the Grüneisen parameter γ has to be estimated independently.

S1.5. Order-Disorder Transition

Thermodynamic properties of minerals with a second-order phase transition or with changes in element ordering between multiple crystallographic sites can be treated with the Landau tricritical theory [e.g., *Carpenter et al.*, 1994; *Holland and Powell*, 1998]. There, standard thermodynamic properties refer to a completely disordered phase (G_{dis}) and a Landau contribution G_{L}, which accounts for progressive ordering with decreasing T, is added to obtain a value for the partially ordered phase (G_{ord}):

$$G_{\mathrm{ord}}(P,T) = G_{\mathrm{dis}}(P,T) + G_{\mathrm{L}}(P,T). \tag{S60}$$

The Landau ordering contribution is applied at temperature below the order-disorder transition $T_{\mathrm{C}}(P)$, defined by the transition temperature at reference pressure $T_{\mathrm{C},0}$ and the Clapeyron slope of the phase transition boundary as:

$$T_{\mathrm{C}}(P) = T_{\mathrm{C},0} + \frac{V_{\mathrm{L,max}}}{S_{\mathrm{L,max}}}P, \tag{S61}$$

where $V_{\mathrm{L,max}}$ is the maximum volume of disorder and $S_{\mathrm{L,max}}$ is the maximum entropy of disorder. At $T < T_{\mathrm{C}}(P)$, the magnitude of ordering is defined by the order parameter Q:

$$Q(P,T) = \sqrt[4]{1 - \frac{T}{T_{\mathrm{C}}(P)}}, \tag{S62}$$

which leads to

$$G_{\mathrm{L}}(P,T) = S_{\mathrm{L,max}} \cdot \left((T - T_{\mathrm{C}}(P))Q(P,T)^2 + \frac{1}{3}T_{\mathrm{C},0}Q(P,T)^6 \right). \tag{S63}$$

The magnitude of the Landau contribution to all thermodynamic properties decreases as Q decreases with increasing temperature; at $T = T_{\mathrm{C}}(P), Q = 0$ and G_{L} vanishes. It is set to zero at $T > T_{\mathrm{C}}(P)$.

Representative thermodynamic properties of the partially ordered phase are obtained by differentiating of Gibbs potential from Equation (S60):

$$V_{\mathrm{ord}}(P,T) = \partial_P G(P,T) \tag{S64}$$
$$= V_{\mathrm{dis}}(P,T) - V_{\mathrm{L,max}}Q(P,T)^2 \cdot \left(1 + \frac{1}{2}\frac{T}{T_{\mathrm{C}}(P)}\left(1 - \frac{T_{\mathrm{C},0}}{T_{\mathrm{C}}(P)}\right)\right), \tag{S65}$$
$$S_{\mathrm{ord}}(P,T) = -\partial_T G(P,T) \tag{S66}$$
$$= S_{\mathrm{dis}}(P,T) - S_{\mathrm{L,max}}Q(P,T)^2 \cdot \left(1 - \frac{1}{2}\left(1 - \frac{T_{\mathrm{C},0}}{T_{\mathrm{C}}(P)}\right)\right), \tag{S67}$$
$$C_{P,\mathrm{ord}}(P,T) = -T\partial_T^2 G(P,T) \tag{S68}$$
$$= C_{P,\mathrm{dis}}(P,T) - \frac{1}{2}S_{\mathrm{L,max}}Q(P,T)^{-2}\frac{T}{T_{\mathrm{C}}(P)} \cdot \left(1 - \frac{1}{2}\left(1 - \frac{T_{\mathrm{C},0}}{T_{\mathrm{C}}(P)}\right)\right). \tag{S69}$$

The Landau model of ordering can generally be applied to any thermodynamic model for pure phases, and in MMA-EoS it is implemented for the Caloric–Murnaghan [*Holland and Powell*, 1998, 2011] and the Birch-Murnaghan–Mie-Grüneisen-Debye equations-of-state [*Stixrude and Lithgow-Bertelloni*, 2011].

S1.6. Solution Phases

The thermodynamic properties of solution phases consist of a linear combination of endmember properties (mixture), configurational (ideal) and excess (non-ideal) mixing contributions [e.g., *Hillert and Staffansson*, 1970; *Ganguly*, 2008]:

$$G = \sum_i x_i G_i - TS_{\mathrm{cf}} + G_{\mathrm{ex}}, \tag{S70}$$
$$S = \sum_i x_i S_i + S_{\mathrm{cf}}, \tag{S71}$$

where i indexes the solution endmembers, G_i and S_i are the standard Gibbs energy and entropy of the i-th endmember, S_{cf} represents the configurational entropy of the solution and G_{ex} is the excess Gibbs energy of mixing. For solutions with linearly independent endmembers, mole fractions are uniquely defined by the bulk solution composition. All solutions treated in this paper are expressed in the linearly independent composition space.

The configurational entropy in the Bragg-Williams approximation is assumed to be statistically random, with mixing of elements or element groups on one or more independent sites that correspond to specific positions in the crystal lattice [*Hillert and Staffansson*, 1970; *Ganguly*, 2008]. The entropy contributions from the individual mixing sites are mutually independent and additive, leading to:

$$S_{\mathrm{cf}} = -R\sum_{s,k} m_s x_{s,k} \ln x_{s,k}, \tag{S72}$$

where m_s represents the multiplicity of site s and $x_{s,k}$ is the mole fraction of constituent k on site s. The fractions $x_{s,k}$ in Equation (S72) can be determined from the endmember mole fractions x_i in Equation (S70) and the site occupancy $N_{i,s,k}$ in formula units of the endmembers:

$$x_{s,k} = \frac{\sum_i N_{i,s,k}}{\sum_{i,k} N_{i,s,k}}, \tag{S73}$$

for any site s and constituent k.

The excess contribution to Gibbs energy of solution has been conventionally expressed by polynomial expansions in terms of endmember or constituent mole fractions [e.g., *Muggianu et al.*, 1975; *Helffrich and Wood*, 1989; *Mukhopadhyay et al.*, 1993], which incorporate several composition schemes for expansion into multicomponent space [*Toop*, 1965; *Pelton*, 2001]. For geological applications, the Kohler-Toop compositional scheme has been widely established implicitly.

The most fundamental approach is a binary symmetric interaction model; with equal number of atoms of the endmembers and negligible differences in ion sizes, the excess energy can be written as

$$G_{\mathrm{ex}}^{(\mathrm{binary})} = \sum_{i<j} x_i x_j W_{i,j}, \tag{S74}$$

where $W_{i,j}$ is the binary interaction energy between the endmembers i and j. MMA-EoS adopts the slightly more complex asymmetric van Laar formulation [*Powell*, 1974; *Holland and Powell*, 2003; *Stixrude and Lithgow-Bertelloni*, 2011], which expands upon the simple two-component case by transforming binary interaction energies into multicomponent space, taking the number of atoms per formula unit of each endmember into account and adding the concept of size parameters:

$$G_{\mathrm{ex}} = \sum_{i<j} \underbrace{\frac{(x_i d_i N_i)(x_j d_j N_j)}{\left(\sum_k x_k d_k N_k\right)^2}}_{=:Y_{i,j}} \cdot \underbrace{2 \cdot \frac{\sum_k x_k d_k}{d_i + d_j} \cdot W_{i,j}}_{=:B_{i,j}}, \tag{S75}$$

where d_i represents a non-dimensional size parameter for the solution component i and the number of atoms per formula unit N_i of endmember i; k ranges over the solution endmembers.

The renormalized interaction energy $B_{i,j}$ in Equation (S75) reduces to $W_{i,j}$ when all size parameters are identical ($d_i = d_j$ for all i, j); this corresponds to the symmetric, regular Margules model, consistent with the energy change due to nearest neighbour energetic interactions [e.g., *Stixrude and Lithgow-Bertelloni*, 2011].

The renormalized product of constituent fractions $Y_{i,j}$ in Equation (S75) reduces to $x_i x_j$ when all size parameters are the same and all solution endmembers have the same number of atoms in a formula unit ($N_i = N_j$ for all i, j). With $Y_{i,j} = x_i x_j$ and $B_{i,j} = W_{i,j}$, Equation (S75) reduces to Equation (S74) for a binary solution.

Intensive material properties of the solution are evaluated as weighted averages of the endmember properties. For example the molar mass and molar volume of the solution are computed as

$$M = \sum_i x_i M_i, \tag{S76}$$

$$V = \sum_i x_i V_i. \tag{S77}$$

Densities and volume derivatives are then found as:

$$\rho = \frac{M}{V}, \tag{S78}$$

$$\alpha = \frac{\sum_i x_i V_i \alpha_i}{V}, \tag{S79}$$

$$\beta = \frac{\sum_i x_i V_i \beta_i}{V}. \tag{S80}$$

An excess volume contribution would have to be added to Equation (S77) in case of P-dependent interaction energies in Equation (S75).

The elastic moduli of the solution are computed as Voigt-Reuss-Hill averages of the endmember properties [*Hill*, 1963]. Given that the endmembers mix on the atomic level and do not act as separate elastic resistors, we weight the modulus averages by mole fractions, consistent with other intensive properties:

$$\kappa = \frac{1}{2}\left(\frac{\sum_i x_i V_i \kappa_i}{V} + \left(\frac{\sum_i x_i V_i \kappa_i^{-1}}{V}\right)^{-1}\right), \tag{S81}$$

where κ_i is the adiabatic bulk modulus of constituent i. An equivalent expression is applied to the calculation of the shear modulus.

S1.7. Multiphase Aggregates

Thermodynamic and other properties of mineral assemblages or multiphase aggregates are computed as linear combinations weighted by *mole amounts* of their constituents, which follows naturally for extensive properties, or by *volume fractions*, which applies to elastic properties that depend on the space occupied by different constituents. This leads to a similar mathematical structure as that used for the computation of solution properties. However, the weighting factors for solutions are generally *mole fractions* and no additional configurational entropy and excess energy terms apply to multiphase aggregates. The aggregate mass and volume of the multiphase aggregate, expressed as extensive properties, become:

$$M_{\text{tot}} = \sum_i X_i M_i, \tag{S82}$$

$$V_{\text{tot}} = \sum_i X_i V_i, \tag{S83}$$

and consequently

$$\rho = \frac{M_{\text{tot}}}{V_{\text{tot}}}, \tag{S84}$$

where i ranges over the phases in the aggregate, X_i is the mole amount, M_i the mass, and V_i the volume of constituent i.

Elastic moduli of the multiphase aggregate are computed as Voigt-Reuss-Hill averages of the single-phase properties [*Hill*, 1963]. However, we weight the moduli of individual phases by *volume fractions* rather than *mole fractions* to account for the distribution of pressure over potentially different types of mineral grains exhibiting different surface areas:

$$\kappa = \frac{1}{2}\left(\frac{\sum_i X_i V_i \kappa_i}{V_{\text{tot}}} + \left(\frac{\sum_i X_i V_i \kappa_i^{-1}}{V_{\text{tot}}}\right)^{-1}\right), \tag{S85}$$

where κ_i is the adiabatic bulk modulus of the i-th constituent. We use an equivalent expression for the calculation of the aggregate shear modulus.

S2. Code Implementation

S2.1. Code Design

All thermodynamic state functions can be derived by differentiating the thermodynamic potential, thus most material properties have closed analytical and self-consistent expressions. This facilitates modular implementation, as the thermodynamic model is an implementation detail that is required to compute values of the desired properties, but the nature of their independent and dependent variables, their general functional form and set of possible computations are known *a-priori*, from general thermodynamic identities. This approach has the advantage that common capabilities of different implementations are controlled by the same commands, making MMA-EoS extensible to additional models without the need to change existing interface or code assembly. In MMA-EoS we have clearly separated interfaces and model implementations, following the structure of the thermodynamic equations (Figure S3).

The principal advantage of such an approach is that little knowledge of the physical model is required to compute individual properties. For example, density is computed the same way for any object, whether it is a single stoichiometric phase, a solution or a polycrystalline aggregate.

S2.2. Language Choice

The high-level aspects of the MMA-EoS software package are implemented in the programming language F# (`http://fsharp.org/`), whereas the LP_SOLVE library benefits from architecture-specific optimizations of arithmetic code, and some interfaces to native system functionality – like MPI – are implemented using C code. The type system of F# specifies physical units of quantities manipulated within the program, offering the guarantee that the code will compile free of unit errors. The code generated by the compiler runs on the CLR virtual machine (MICROSOFT) with automatic memory management and portability to different operating systems. The language F# can be used as an interpreter, so programming interfaces offered by MMA-EoS can easily be scripted or be used interactively for small calculations. At the same time, MMA-EoS includes a set of command line programs that handle common computation tasks, as documented in the distribution of the code (`https://bitbucket.org/chust/eos`).

We have implemented a number of unit tests in MMA-EoS to verify its functionality, internal consistency and physically sensible behavior of its components. For each thermodynamic model implemented, the tests check, for instance, that the molar volume of a substance decreases with pressure, and verifies that fundamental thermodynamic identities such as $V = \partial_P G$ hold numerically. The automated tests also include comparisons of key parameters to experimental data. However, no quantitative assessment of the results and their accuracy is performed.

S2.3. Numerical Details

Non-analytical solutions to the equations-of-state are found numerically in the MMA-EoS software. The code uses interval bisection, which allows error estimation and refinement of the result to a high accuracy. The initial interval (minimum and maximum value) is prescribed to cover a wide range of physically sensible volumes.

The computation of some thermodynamic state functions, e.g. $V(P,T) = \partial_P G(P,T)$ and $S(P,T) = -\partial_T G(P,T)$, is performed numerically when non-analytical expressions are involved. We perform numerical differentiation using an adaptive scheme that combines a second-order approximation with higher orders to obtain both a value of the derivative and an error estimate. For two-sided derivatives we combine second- and fourth-order schemes, for one-sided derivatives (for instance, at the lower temperature limit) we combine second- and third-order schemes. The step length in numerical differentiation is reduced exponentially until the desired accuracy has been achieved, or a minimum step length to prevent rounding errors has been reached. In general, the desired accuracy is at least two orders of magnitude lower than the derivative value. As an example, for the numerical differentiation of G by P to obtain V, the desired accuracy is set to $10^{-8}\,\mathrm{m^3\ mol^{-1}}$ and the minimum step length to 10^5 Pa.

Approximations to the Debye integral are calculated using Chebyshev polynomials and half-analytical expressions that depend on the magnitude of the argument $x = \theta_D/T$ in Equation (S40).

Other numerically evaluated integrals are computed with an adaptive Gauss-Kronrod scheme, which combines seven- and fifteen-point quadrature rules in order to obtain the integral value and its error estimate simultaneously. The integration interval is progressively split such that the error estimate for each segment becomes lower than a desired threshold, with a lower limit on the segment length set to restrict the effect of rounding errors. The maximum and minimum step length are estimated as

$$\Delta x_{\max} = \frac{x_{\max} - x_{\min}}{2} \tag{S86}$$

and

$$\Delta x_{\min} = \sqrt{\frac{\Delta I}{\Delta x_{\max}}}\Delta x_{\max}, \tag{S87}$$

where $x_{\max}$ and $x_{\min}$ are the integration boundaries and ΔI is the desired maximum error per segment. For example, we use the maximum error per segment $\Delta I = 1\ \mathrm{J\ mol^{-1}}$ when integrating Equation (S5).

The search for the equilibrium phase assemblage is treated as an optimization problem in MMA-EoS. The Gibbs energy of the system consisting of all candidate phases forms a linear objective function,

$$G = \sum_i^{\text{phases}} (n_i G_i), \tag{S88}$$

where n_i is the (positive) number of moles of phase i. The minimizer assumes P and T to be free variables not subject to further constraints, so the phase rule requires that the number of phases that have non-zero amounts corresponds to the number of independent system components. The objective function is minimized with one free variable (n_i) at a time, subject to bulk composition constraints. These constraints are the mass balance relationships for each chemical component of the system and they can be represented as an equality or inequality relation. In the latter case, the phase set hosts smaller amounts of the chemical component than available, and this situation arises where part of the composition space is not covered by any phase.

Our implementation uses a bundled version of the LP_SOLVE library to optimize the objective function under mass-balance constraints. The algorithm scales the linear optimization problem to numerically convenient value ranges, which makes the solution independent of any multipliers in mass-balance constraints, i.e., independent of the choice of the chemical-formula size (e.g., $MgSiO_3$ and $Mg_4Si_4O_{12}$ are equivalent). Simultaneously with the linear optimization to find the stable phase assemblage, MMA-EoS locates the optimal composition of solution phases as a non-linear optimization problem. Combinations of phases that can represent the bulk composition are selected, and the energetically most favorable set is determined. The initial selection uses the endmembers of the solid solutions and, in a non-linear optimization task, the solution composition is modified with the steepest-descent method. The composition space of the solid solution is discretized into hypothetical intermediate phases (pseudocompounds), and their compositions are modified until a local minimum is attained. The new candidates are added to the set of plausible phases before a new iteration step of the linear optimization is performed. The size of composition steps for the steepest-descent method search can be adapted, the default value is 0.4 mol%.

The LP_SOLVE library employs the simplex method to find an optimal solution, iterating through the nodes of the polytope consisting of all vectors of modal amounts in the c-dimensional space defined by c linear inequalities. Each such node represents a feasible, but not necessarily optimal solution to the problem. The algorithm moves between neighbouring nodes sharing $p - 1$ phases, thus changing one coordinate (modal amount of a phase) at a time, such that the objective value does not increase in any step [*Dantzig*, 1963].

S3. Application of Thermodynamic Models

S3.1. Gibbs Energy

Values and uncertainties of volumetric and caloric properties propagate through integration into the Gibbs energy of a phase (Equations (S1), (S2), (S3), (S5), (S22), (S28), (S32) and (S35)) that is essential for an accurate calculation of phase equilibria. Individual uncertainties are partially reduced due to inherent correlations in thermodynamic properties resulting from a large number of degrees of freedom, and therefore depend on the approach used in the construction of a specific thermodynamic dataset. We illustrate these features by comparing the difference between Gibbs energy of the models and assessments by *Stixrude and Lithgow-Bertelloni* [2011] and *Holland et al.* [2013] from ambient conditions to 3000 K and 26 GPa for the Mg_2SiO_4 and Fe_2SiO_4 polymorphs (Figure S4).

For the Mg_2SiO_4 phases, the differences in Gibbs energy (ΔG) of forsterite, wadsleyite and ringwoodite between the databases of *Stixrude and Lithgow-Bertelloni* [2011] and *Holland et al.* [2013] do not exceed 1 kJ mol^{-1} atom^{-1} in general, over the whole P-T range considered (Figure S4), which is comparable to the nominal accuracy of internally consistent thermodynamic datasets. In particular, ΔG remains negligible (< 0.2 kJ mol^{-1} atom^{-1}) during compression to 26 GPa at ambient T (Figure S4). This indicates that the performance of the Modified-Tait and Birch-Murnaghan equations-of-state is essentially identical for the purpose of phase equilibrium calculations. By contrast, ΔG during heating at ambient P either systematically increases or reaches a broad maximum between 1000 and 2000 K. This behavior is related to functional differences in the heat capacity models (empirical polynomial *vs.* Debye treatment) as discussed in Section 4.1.2 (Figures 3 and 4), and illustrates persistent discrepancies in the caloric characterization of condensed phases at moderate and high T.

Insufficient or discrepant calibrations of compression or caloric properties tend to dominate ΔG pattern in P-T space in a linear manner, as illustrated for the Fe_2SiO_4 polymorphs (Figure S4). In all three cases, the Gibbs energy difference is dominated by T dependence: it increases nearly linearly with T and reaches values of $\sim$ 15 kJ mol^{-1} atom^{-1} K^{-1} at 3000 K. The steep, nearly linear increase of ΔG reflects the fact that the entropies of the Fe_2SiO_4 polymorphs in the models and assessments of *Stixrude and Lithgow-Bertelloni* [2011] and *Holland et al.* [2013] differ substantially (Figure 3). The similar magnitude of uncertainties for all polymorphs indicates that this deficiency does not primarily affect the phase equilibria in the one-component system Fe_2SiO_4, but plays a significant role in the Mg_2SiO_4-Fe_2SiO_4 solution or any more complex systems at high T as discussed in Section 4.3.2. Similar to the Mg_2SiO_4 polymorphs, the Gibbs energy differences for the Fe_2SiO_4 phases do not exceed 0.5 kJ mol^{-1} atom^{-1} during isothermal compression to 26 GPa.

S3.2. Configurational Properties

MMA-EoS uses the Bragg-Williams approximation to random distribution of atoms and their groups to compute the configurational entropy of solution phases (Section S1.6). Contributions to S_{cf} from independent mixing sites are additive and proportional to the multiplicity of each site. The formulation of configurational properties becomes non-unique when partial ordering on one or more crystallochemical sites is considered. To implement ordering schemes, we introduce the following notation of nested parentheses for use in MMA-EoS: the first (outer) level of parentheses $(\ldots)_n$ designates a mixing site and the associated subscript n represents the mixing multiplicity (suppressed notation implies a multiplicity of one). The element amounts on a site is allowed to become fractional numbers. A second (inner) level of parentheses $((\ldots))_n$ encloses groups of atoms that are considered to be a single entity for the purpose of configurational entropy calculations.

Consider the clinopyroxene binary solution between the diopside $CaMgSi_2O_6$ (di) and Ca-tschermak $CaAlAlSiO_6$ (cats) endmembers. The solid solution consists of three mixing sites – M2, M1 and T with the mixing multiplicities of one, one and two, respectively – per six-oxygen formula unit [*Putnis*, 1992]. Figure S5 compares various scenarios for Al-Si distribution on the tetrahedral site of clinopyroxene in the literature [*Gasparik*, 1984; *Cohen*, 1986; *Vinograd*, 2001]:

(i) Random mixing of Mg and Al on the M1 octahedral site and of Al and Si on the tetrahedral site with a mixing multiplicity n=2, represented by the solution formula $Ca(Mg,Al)(Al,Si)_2O_6$ and shown in the solid blue line in Figure S5. The configurational entropy of the diopside-Ca-tschermak solid solution becomes:

$$\begin{aligned} S_{\mathrm{cpx}} = -R\cdot &\left(x \ln x + (1-x)\ln(1-x) + 2\frac{x}{2}\ln\frac{x}{2}\right.\\ &\left. + 2\left(1-\frac{x}{2}\right)\ln\left(1-\frac{x}{2}\right)\right), \end{aligned} \tag{S89}$$

where x is the mole fraction of Ca-tschermak. The configurational contribution to the Ca-tschermak endmember resulting from Al-Si disorder is

$$\begin{aligned} S_{\mathrm{cats}} &= -R\cdot 2\cdot\left(\frac{1}{2}\ln\frac{1}{2} + \frac{1}{2}\ln\frac{1}{2}\right)\\ &\approx 1.15\ \mathrm{J\ K^{-1}\ mol^{-1}\ atom^{-1}}. \end{aligned} \tag{S90}$$

(ii) Random mixing of Mg and Al on the M1 octahedral site and ordering of Al and Si on the tetrahedral sites, subject to the Al-avoidance principle [*Loewenstein*, 1954]. This requirement is analogous to formally splitting the tetrahedral sites into T2, hosting Si and Al, and T1, occupied by Si only. This element allocation is represented by the solution formula $Ca(Mg,Al)(Al,Si)SiO_6$ (solid green line in Figure S5). The configurational entropy of the diopside-Ca-tschermak solution is then defined as:

$$\begin{aligned} S_{\mathrm{cpx}} = -R\cdot &(x\ln x + (1-x)\ln(1-x)\\ &+ x\ln x + (1-x)\ln(1-x)). \end{aligned} \tag{S91}$$

There is no configurational contribution to the entropy of Ca-tschermak in this model as all sites are occupied by one element only. The results of this scenario, however, contradicts previous experimental measurements and thermodynamic assessments [*Gasparik*, 1984; *Cohen*, 1986; *Vinograd*, 2001].

Intermediate configurational entropy of the Ca-tschermak endmember can be obtained by adopting partial order in the tetrahedral site or by charge coupling between the tetrahedral and octahedral sites.

(iii) The Al-avoidance rule for the tetrahedral site is partially taken into account by assuming Al-Si avoidance on the T1 site and Al-Si disorder on the T2 site. This situation corresponds to an alternation of chains with disordered and partially ordered aluminosilicate tetrahedra, respectively, and is expressed by the solution formula $Ca(Mg,Al)(Si,Al)(Si_{\frac{1}{2}}Al_{\frac{1}{2}})Si_{\frac{1}{2}}O_6$; the site allocation for the Ca-tschermak endmember becomes $Ca(Al)(Al_{\frac{1}{2}}Si_{\frac{1}{2}})(Al)_{\frac{1}{2}}Si_{\frac{1}{2}}O_6$ (solid magenta line in Figure S5). The element fractions on the T2 site are related to the mole fraction of Ca-tschermak by $x_{\mathrm{Al,T2}} = \frac{x}{2}$ and $x_{\mathrm{Si,T2}} = 1 - \frac{x}{2}$. The configurational entropy of the diopside-Ca-tschermak solution is then calculated as:

$$\begin{aligned} S_{\mathrm{cpx}} = -R\cdot &(x\ln x + (1-x)\ln(1-x)\\ &+ \frac{1}{2}(x\ln x + (1-x)\ln(1-x))\\ &+ \frac{1}{2}\left(\frac{x}{2}\ln\frac{x}{2} + \left(1-\frac{x}{2}\right)\ln\left(1-\frac{x}{2}\right)\right)\Bigg). \end{aligned} \tag{S92}$$

Consequently, the Ca-tschermak entropy is

$$\begin{aligned} S_{\mathrm{cats}} &= -R\cdot\left(\frac{1}{2}\ln\frac{1}{2} + \frac{1}{2}\ln\frac{1}{2}\right)\\ &\approx 0.58\ \mathrm{J\ K^{-1}\ mol^{-1}\ atom^{-1}}. \end{aligned} \tag{S93}$$

In all three models, the requirement of local charge balance may further reduce site depends on the Al-Si distribution in the tetrahedral site(s). The charge balance constraint does not affect S_{cf} of Ca-tschermak, but decreases it by 1/2 at the center of the binary join (Figure S5, dashed curves).

These considerations illustrate that simple Bragg-Williams models offer a sufficient range of versatility to reproduce simulation results or experimental data. In particular the ionic disordered case (scenario i) is within the error interval given by *Cohen* [1986].

S3.3. Phase Equilibria for $Mg_2Si_2O_6$-$CaMgSi_2O_6$

The system $Mg_2Si_2O_6$-$CaMgSi_2O_6$ provides an example with complex, reciprocal solution models and pseudo-binary mineral stabilities (e.g., garnet). Using the database by *Stixrude and Lithgow-Bertelloni* [2011], the pyroxene endmembers are predicted stable up to 16 GPa at $T = 1923$ K (Figure S6). For enstatite, phases occur according to the $MgSiO_3$ phase diagram (Figure 6). On the diopside side, Ca-perovskite forms at $P > 12$ GPa and high Ca-concentrations. Above 18 GPa it extends to a wide composition rage, consistent with the assessment by *Gasparik* [2003] and experimental data on diopside [*Canil*, 1994; *Akaogi et al.*, 2004]. In addition, garnet is predicted to be stable between 16 and 20 GPa and $x_{\mathrm{Ca}} \leq 0.80$, over a slightly larger composition range than in the assessment by *Gasparik* [2003], probably due to the fact that the CM phase described by *Gasparik* [1990a, b] is not included in the assessment of *Stixrude and Lithgow-Bertelloni* [2011]. Above 20 GPa, garnet transforms to akimotoite (20 GPa) and then to bridgmanite (22 GPa), consistent with the thermodynamic assessment of the system [*Gasparik*, 2003] and experiments by *Akaogi et al.* [2004] on diopside.

S3.4. Elasticity of Garnets

We illustrate the application of the thermoelastic model of *Stixrude and Lithgow-Bertelloni* [2011] for density and elastic properties (shear and bulk modulus) in three garnet binary solutions that play a central role through the upper mantle and the transition zone (Figures 9, 13 and 16): $Mg_3Al_2Si_3O_{12}$-$Fe_3Al_2Si_3O_{12}$ (pyrope-almandine), $Mg_3Al_2Si_3O_{12}$-$Ca_3Al_2Si_3O_{12}$ (pyrope-grossular) and $Mg_3Al_2Si_3O_{12}$-$Mg_4Si_4O_{12}$ (pyrope-majorite). The agreement of density with data from ambient to high pressures is very good overall (Figures S7).

Elastic moduli of the garnet binaries at elevated pressures show significantly larger scatter around the values computed with the database of *Stixrude and Lithgow-Bertelloni* [2011] (Figures S7), most prominently along the pyrope-majorite join with a large number of experimental studies. Experimental measurements for pyrope by *Gwanmesia et al.* [2006]; *Zou et al.* [2012] and *Chantel* [2012] show significantly differing P-dependence for both the shear and bulk modulus. In addition, the reference values of the bulk and shear moduli at ambient pressure differ between the experiments of *Sinogeikin and Bass* [2002a]; *Gwanmesia et al.* [2006] and *Chantel* [2012] by as much as 10 GPa and 6 GPa, respectively. Across the solution, moduli of most studies [*Pamato et al.*, 2016; *Sinogeikin and Bass*, 2002a; *Liu et al.*, 2015] agree reasonably well with the model predictions of *Stixrude and Lithgow-Bertelloni* [2011], while values of *Chantel* [2012] are significantly lower and those of *Gwanmesia et al.* [2009] significantly larger.

Although these discrepancies likely stem from uncertainties in the experimental data, it is possible – in principle – that the elastic parameters show non-linear dependence that is not captured by the quasi-linear formulation of elasticity in the mixing model (Equation (S81)). In order to accommodate the non-linear behavior, the model formulation would need to be modified. However, the possibility of non-linear elastic behavior across a solid solution remains an open question, even at ambient conditions for a well studied system such as grossular-andradite [*O'Neill et al.*, 1989; *Lacivita et al.*, 2014].

S4. Additional Phase Diagrams

S4.1. Reduced Pyrolite Compositions

Phase diagrams for the reduced pyrolite compositions (Table 2) FMS (Figure S8), CFMS (Figure S9) and CFMAS (Figure S10) are included to complement the phase proportions plots (Figure 9) in the main text, and as a comparison to the full phase diagrams for the reduced MS, FMAS and NCFMAS systems shown there (Figures 10-12).

S4.2. Phase Diagrams for Slab Lithologies

Similarly, the full phase diagram for the depleted mantle (Figure S11) and bulk oceanic crust (Figure S12) slab lithologies (Table 2) are included in the supporting online material as a complement to the phase proportion plots shown in the main text (Figure 16).

We have observed large differences for the phase diagrams for bulk oceanic crust (Table 2) predicted with the database of *Stixrude and Lithgow-Bertelloni* [2011] (Figure S12) and that of basalt in *Xu et al.* [2008]. In order to compare and analyze these discrepancies we have performed four sets of calculations, using the databases of *Stixrude and Lithgow-Bertelloni* [2011] and *Xu et al.* [2008] and two different sets of basalt compositions: bulk oceanic crust of *Chemia et al.* [2015] and basalt of *Presnall and Hoover* [1987]. Using the database of *Xu et al.* [2008] and the basalt composition of *Presnall and Hoover* [1987], we reproduce the phase diagram of *Xu et al.* [2008] well (Figure S13).

S5. Adiabatic gradients in the mantle

To complement the isentropic T-profiles computed self-consistently with the thermodynamic database of *Stixrude and Lithgow-Bertelloni* [2011] (Figure 17) and to facilitate a comparison to *Katsura et al.* [2010], the adiabatic gradient for isentropes with a potential temperature of 1600 K are calculated for pyrolite, depleted mantle and bulk oceanic crust lithologies by numerical differentiation (Figure S14).

References

Akaogi, M., M. Yano, Y. Tejima, M. Iijima, and H. Kojitani (2004), High-pressure transitions of diopside and wollastonite: Phase equilibria and thermochemistry of $CaMgSi_2O_6$, $CaSiO_3$ and $CaSi_2O_5$ - $CaTiSiO_5$ system, *Physics of the Earth and Planetary Interiors*, *143-144*, 145–156.

Ashcroft, N. W., and N. D. Mermin (1976), *Solid State Physics*, Saunders, Philadelphia.

Bale, C., P. Chartrand, S. Degterov, G. Eriksson, K. Hack, R. B. Mahfoud, J. Melançon, A. Pelton, and S. Petersen (2002), Factsage thermochemical software and databases, *Calphad*, *26*(2), 189–228.

Birch, F. (1947), Finite elastic strain of cubic crystals, *Physical Review*, *71*(11), 809–824, doi:10.1103/PhysRev.71.809.

Canil, D. (1994), Stability of clinopyroxene at pressure-temperature conditions of the transition region, *Physics of the Earth and Planetary Interiors*, *86*, 25–34.

Carpenter, M. A., R. Powell, and E. K. Salje (1994), Thermodynamics of nonconvergent cation ordering in minerals; I, an alternative approach, *American Mineralogist*, *79*(11-12), 1053–1067.

Chantel, J. (2012), Measurement of elastic properties of silicates at realistic mantle pressures, Ph.D. thesis, Universität Bayreuth.

Chemia, Z., D. Dolejš, and G. Steinle-Neumann (2015), Thermal effects of variable material properties and metamorphic reactions in a three-component subducting slab, *Journal of Geophysical Research*, *120*, 6823–6845, doi:10.1002/2015JB012080.

Cohen, R. E. (1986), Thermodynamic solution properties of aluminous clinopyroxenes: Nonlinear least squares refinements, *Geochimica et Cosmochimica Acta*, *50*, 563–575, doi:10.1016/0016-7037(86)90105-5.

Dantzig, G. B. (1963), *Linear Programming and Extensions*, Princeton University Press.

Debye, P. (1912), Zur Theorie der spezifischen Wärmen, *Annalen der Physik*, *344*(14), 789–839, doi:10.1002/andp.19123441404.

Fabrichnaya, O., S. K. Saxena, P. Richet, and E. F. Westrum (2004), *Thermodynamic Data, Models, and Phase Diagrams in Multicomponent Oxide Systems*, Springer Verlag.

Fan, D. W., W. G. Zhou, C. Q. Liu, Y. G. Liu, F. Wan, Y. S. Xing, J. Liu, L. G. Bai, and H. S. Xie (2009), The thermal equation of state of $(Fe_{0.86}Mg_{0.07}Mn_{0.07})_3Al_2Si_3O_{12}$ almandine, *Mineralogical Magazine*, *73*(1), 95–102, doi:10.1180/minmag.2009.073.1.95.

Ganguly, J. (2008), *Thermodynamics in Earth and Planetary Sciences*, Springer-Verlag Berlin Heidelberg, doi:10.1007/978-3-540-77306-1.

Gasparik, T. (1984), Experimentally determined stability of clinopyroxene + garnet + corundum in the system CaO-MgO-Al_2O_3-SiO_2, *American Mineralogist*, *69*, 1025–1035.

Gasparik, T. (1990a), Phase-relations in the transition zone, *Journal of Geophysical Research*, *95*(B10), 15,751–15,769.

Gasparik, T. (1990b), A thermodynamic model for the enstatite – diopside join, *American Mineralogist*, *75*(9-10), 1080–1091.

Gasparik, T. (2003), *Phase Diagrams for Geoscientists – An Atlas of the Earth's Interior*, 2nd ed., Springer Verlag.

Gréaux, S., Y. Kono, N. Nishiyama, T. Kunimoto, K. Wada, and T. Irifune (2011), *P-V-T* equation of state of $Ca_3Al_2Si_3O_{12}$ grossular garnet, *Physics and Chemistry of Minerals*, *38*, 85–94, doi:10.1007/s00269-010-0384-1.

Gwanmesia, G. D., G. Chen, and R. C. Liebermann (1998), Sound velocities in $MgSiO_3$-garnet to 8 GPa, *Geophysical Research Letters*, *25*(24), 4553–4556, doi:10.1029/1998GL900189.

Gwanmesia, G. D., J. Zhang, K. Darling, J. Kung, B. Li, L. Wang, D. Neuville, and R. C. Liebermann (2006), Elasticity of polycrystalline pyrope $Mg_3Al_2Si_3O_{12}$ to 9 GPa and 1000 °C, *Physics of the Earth and Planetary Interiors*, *155*, 179–190, doi:10.1016/j.pepi.2005.10.008.

Gwanmesia, G. D., L. Wang, R. Triplett, and R. C. Liebermann (2009), Pressure and temperature dependence of the elasticity of pyrope-majorite [$py_{60}mj_{40}$ and $py_{50}mj_{50}$] garnets solid solution measured by ultrasonic interferometry technique, *Physics of the Earth and Planetary Interiors*, *174*, 105–112, doi:10.1016/j.pepi.2008.07.029.

Helffrich, G., and B. J. Wood (1989), Subregular model for multicomponent solutions, *American Mineralogist*, *74*(9-10), 1016–1022.

Hill, R. (1963), Elastic properties of reinforced solids: Some theoretical principles, *Journal of the Mechanics and Physics of Solids*, *11*(5), 357–372, doi:10.1016/0022-5096(63)90036-X.

Hillert, M., and L.-I. Staffansson (1970), The regular solution model for stoichiometric phases and ionic melts, *Acta Chemica Scandinavica*, *24*, 3618–3626, doi:10.3891/acta.chem.scand.24-3618.

Holland, T., and R. Powell (2003), Activity–composition relations for phases in petrological calculations: an asymmetric multicomponent formulation, *Contributions to Mineralogy and Petrology*, *145*(4), 492–501, doi:10.1007/s00410-003-0464-z.

Holland, T. J. B., and R. Powell (1998), An internally consistent thermodynamic data set for phases of petrological interest, *Journal of Metamorphic Geology*, *16*, 309–343.

Holland, T. J. B., and R. Powell (2011), An improved and extended internally consistent thermodynamic dataset for phases of petrological interest, involving a new equation of state for solids, *Journal of Metamorphic Geology*, *29*, 333–383, doi:10.1111/j.1525-1314.2010.00923.x.

Holland, T. J. B., N. F. C. Hudson, R. Powell, and B. Harte (2013), New thermodynamic models and calculated phase equilibria in NCFMAS for basic and ultrabasic compositions through the transition zone into the uppermost lower mantle, *Journal of Petrology*, *54*(9), 1901–1920, doi:10.1093/petrology/egt035.

Huang, S., and J. Chen (2014), Equation of state of pyrope-almandine solid solution measured using a diamond anvil cell and in situ synchrotron x-ray diffraction, *Physics of the Earth and Planetary Interiors*, *228*, 88–91, doi:10.1016/j.pepi.2014.01.014.

Ita, J., and L. Stixrude (1992), Petrology, elasticity and composition of the mantle transition zone, *Journal of Geophysical Research*, *97*(B5), 6849–6866.

Katsura, T., A. Yoneda, D. Yamazaki, T. Yoshino, and E. Ito (2010), Adiabatic temperature profile in the mantle, *Physics of the Earth and Planetary Interiors*, *183*, 212–218, doi:10.1016/j.pepi.2010.07.001.

Kono, Y., S. Gréaux, Y. Higo, H. Ohfuji, and T. Irifune (2010), Pressure and temperature dependences of elastic properties of grossular garnet up to 17 GPa and 1650 K, *Journal of Earth Science*, *21*(5), 782–791, doi:10.1007/s12583-010-0112-2.

Lacivita, V., A. Erba, R. Dovesi, and P. D'Arco (2014), Elasticity of grossular-andradite solid solution: an ab initio investigation, *Physical Chemistry, Chemical Physics*, *16*(29), 15,331–15,338.

Liu, Z., T. Irifune, S. Gréaux, T. Arimoto, T. Shinmei, and Y. Higo (2015), Elastic wave velocity of polycrystalline $Mj_{80}Py_{20}$ garnet to 21 GPa and 2000 K, *Physics and Chemistry of Minerals*, *42*, 213–222, doi:10.1007/s00269-014-0712-y.

Loewenstein, W. (1954), Configurational entropy of binary silicate solid solutions, *American Mineralogist*, *39*, 92–96.

Matas, J. (1999), Modélisation thermochimique des propriétés de solides a hautes températures et hautes pressions, Ph.D. thesis, Charles University Prague and École Normale Supérieur Lyon.

Morishima, H., E. Ohtani, T. Kato, T. Kubo, A. Suzuki, T. Kikegawa, and O. Shimomura (1999), The high-pressure and temperature equation of state of a majorite solid solution in the system of $Mg_4Si_4O_{12}$-$Mg_3Al_2Si_3O_{12}$, *Physics and Chemistry of Minerals*, *27*, 3–10.

Muggianu, Y.-M., M. Gambino, and J.-P. Bros (1975), Enthalpies de formation des alliages liquides Bismuth-Étain-Gallium à 723 K. choix d'une représentation analytique des grandeurs d'excès intégrales et partielles de mélange, *Journal de Chimie Physique et de Physico-Chimie Biologique*, *72*(1), 83–88.

Mukhopadhyay, B., S. Basu, and M. J. Holdaway (1993), A discussion of Margules-type formulations for multicomponent solutions with a generalized approach, *Geochimica et Cosmochimica Acta*, *57*(2), 277–283, doi:10.1016/0016-7037(93)90430-5.

Murnaghan, F. D. (1944), The compressibility of media under extreme pressures, *Proceedings of the National Academy of Sciences of the United States of America*, *30*, 244–247.

O'Neill, B., J. Bass, J. Smyth, and M. Vaughan (1989), Elasticity of a grossular-pyrope-almandine garnet, *Journal of Geophysical Research*, *94*, 17,819, doi:10.1029/JB094iB12p17819.

Pamato, M. G., A. Kurnosov, T. B. Ballaran, D. J. Frost, L. Ziberna, M. Giannini, S. Speziale, S. N. Tkachev, K. K. Zhuravlev, and V. B. Prakapenka (2016), Single crystal elasticity of majoritic garnets: Stagnant slabs and thermal anomalies at the base of the transition zone, *Earth and Planetary Science Letters*, *451*, 114–124, doi:10.1016/j.epsl.2016.07.019.

Pavese, A., V. Diella, V. Pischedda, M. Merli, R. Bocchio, and M. Mezouar (2001), Pressure-volume-temperature equation of state of andradite and grossular, by high-pressure and -temperature powder diffraction, *Physics and Chemistry of Minerals*, *28*, 242–248.

Pelton, A. D. (2001), A general "geometric" thermodynamic model for multicomponent solutions, *Calphad*, *25*(2), 319–328, doi:10.1016/S0364-5916(01)00052-9.

Piazzoni, A. S., G. Steinle-Neumann, H.-P. Bunge, and D. Dolejš (2007), A mineralogical model for density and elasticity of the Earth's mantle, *Geochemistry, Geophysics, Geosystems*, *8*(11), Q11,010, doi:10.1029/2007GC001697.

Poirier, J.-P. (2000), *Introduction to the Physics of the Earth's Interior*, 2 ed., Cambridge University Press.

Powell, R. (1974), A comparison of some mixing models for crystalline silicate solid solutions, *Contributions to Mineralogy and Petrology*, *46*(4), 265–274, doi:10.1007/BF00370967.

Presnall, D. C., and J. D. Hoover (1987), High pressure phase equilibrium constraints on the origin of mid-ocean ridge basalts, in *Magmatic processes: Physicochemical Principles*, vol. 1, pp. 75–88, Geochemical Society University Park, Pa.

Putnis, A. (1992), *An introduction to mineral sciences*, Cambridge University Press.

Sinogeikin, S. V., and J. D. Bass (2002a), Elasticity of pyrope and majorite-pyrope solid solutions to high temperatures, *Earth and Planetary Science Letters*, *203*, 549–555, doi: doi:10.1016/S0012-821X(02)00851-8.

Sinogeikin, S. V., and J. D. Bass (2002b), Elasticity of majorite and a majorite-pyrope solid solution to high pressure: Implications for the transition zone, *Geophysical Research Letters*, *29*(2), 1017, doi:doi:10.1029/2001GL013937.

Stixrude, L., and C. Lithgow-Bertelloni (2005), Thermodynamics of mantle minerals – I. Physical properties, *Geophysical Journal International*, *162*, 610–632, doi:10.1111/j.1365-246X.2005.02642.x.

Stixrude, L., and C. Lithgow-Bertelloni (2011), Thermodynamics of mantle minerals – II. Phase equilibria, *Geophysical Journal International*, *184*, 1180–1213, doi:10.1111/j.1365-246X.2010.04890.x.

Toop, G. W. (1965), Predicting ternary activities using binary data, *Transactions of the Metallurgical Society of AIME*, *233*, 850–855.

Vinograd, V. L. (2001), Configurational entropy of binary solid solutions, in *EMU Notes in Mineralogy: Solid solutions in silicate and oxide systems*, vol. 3, chap. 12, pp. 303–346, Eötvös University Press, Budapest.

Xu, W., C. Lithgow-Bertelloni, L. Stixrude, and J. Ritsema (2008), The effect of bulk composition and temperature on mantle seismic structure, *Earth and Planetary Science Letters*, *275*, 70–79, doi:10.1016/j.epsl.2008.08.012.

Zhang, L., H. Ahsbahs, A. Kutoglu, and C. Geiger (1999), Single-crystal hydrostatic compression of synthetic pyrope, almandine, spessartine, grossular and andradite garnets at high pressures, *Physics and Chemistry of Minerals*, *27*, 52–58.

Zou, Y., T. Irifune, S. Gréaux, M. L. Whitaker, T. Shinmei, H. Ohfuji, R. Negishi, and Y. Higo (2012), Elasticity and sound velocities of polycrystalline $Mg_3Al_2(SiO_4)_3$ garnet up to 20 GPa and 1700 K, *Journal of Applied Physics*, *112*, 014,910, doi:10.1063/1.4736407.

Corresponding author: T. C. Chust, Bayerisches Geoinstitut, Universität Bayreuth, 95440 Bayreuth, Germany. (thomas.chust@uni-bayreuth.de)

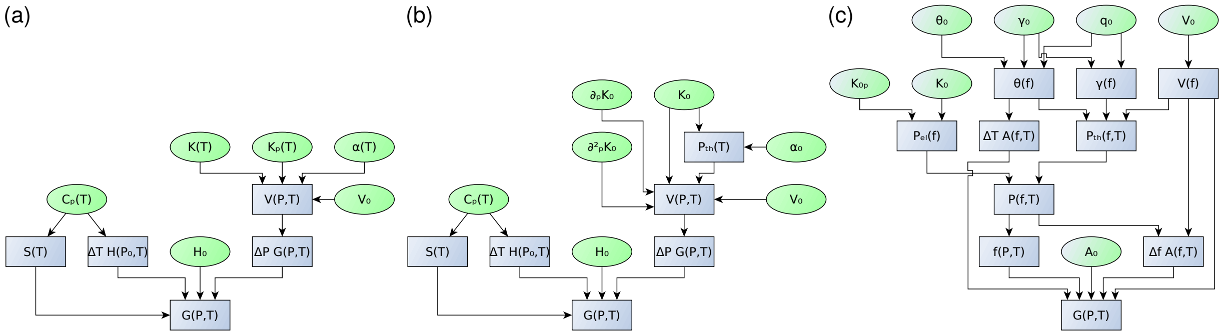

Figure S1: Data flow in (a) the Caloric–Murnaghan model, (b) the Caloric–Modified-Tait model and (c) the Birch-Murnaghan–Mie-Grüneisen-Debye model for the computation of Gibbs energy used by *Fabrichnaya et al.* [2004], *Holland et al.* [2013] and *Stixrude and Lithgow-Bertelloni* [2011], respectively. Gibbs energy G is assembled from an elastic part $\Delta P\, G(P,T) = [G(P,T)]_{P_0}^{P}$ or $\Delta f\, A(f,T) = [A(f,T)]_{f(V_0)}^{f(V)}$, following (a) the Murnaghan, (b) Tait or (c) Birch-Murnaghan formalism, and a thermal part $\Delta T\, H(P,T) = [H(P,T)]_{T_0}^{T}$ or $\Delta T\, A(f,T) = [A(f,T)]_{T_0}^{T}$, based on a polynomial representation of the heat capacity (a, b) or the Debye model (c). Model parameters (taken from a database of phases at runtime) are enclosed in ellipses and shaded green while the computational steps of the model code are represented by rectangular boxes shaded blue; model parameters that are functions of T in panels (a) and (b) are polynomials in T. Abbreviations for physical parameters used in the flow chart are listed in Table 1.

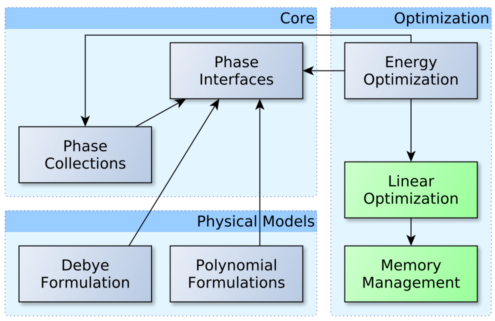

Figure S2: Module structure of the MMA-EoS software library. The diagram shows functional units as boxes and direct dependencies as arrows. Blue boxes represent functionality implemented in the F# language, while green boxes represent code written in the programming language C.

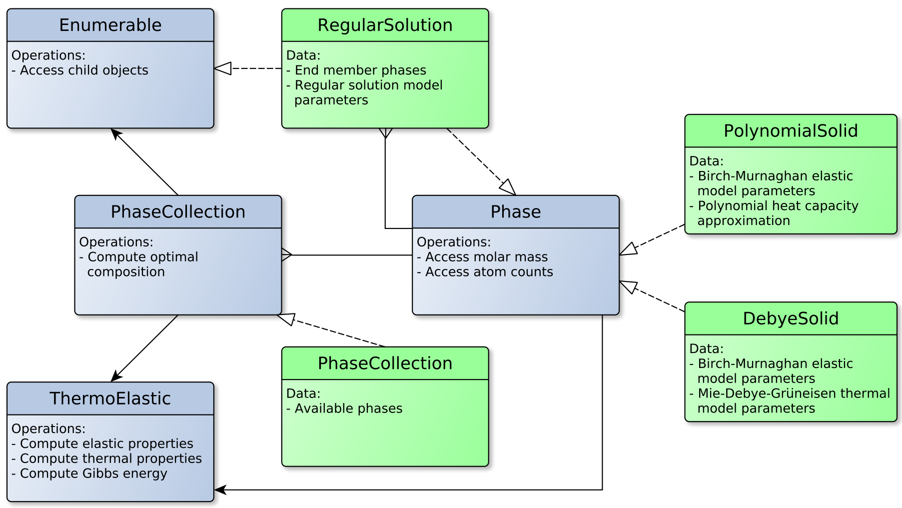

Figure S3: Interface structure of the MMA-EoS software library. The diagram shows programming interfaces and their relations: Boxes with blue background represent interfaces to common functionality while boxes with green background represent implementations of these interfaces. Solid arrows link interfaces to "parents", i.e., more general interfaces whose functionality is implied by the more specific ones. Dashed arrows link implementations to their supported interfaces. Solid lines with an arrow head at the start represent aggregation relationships.

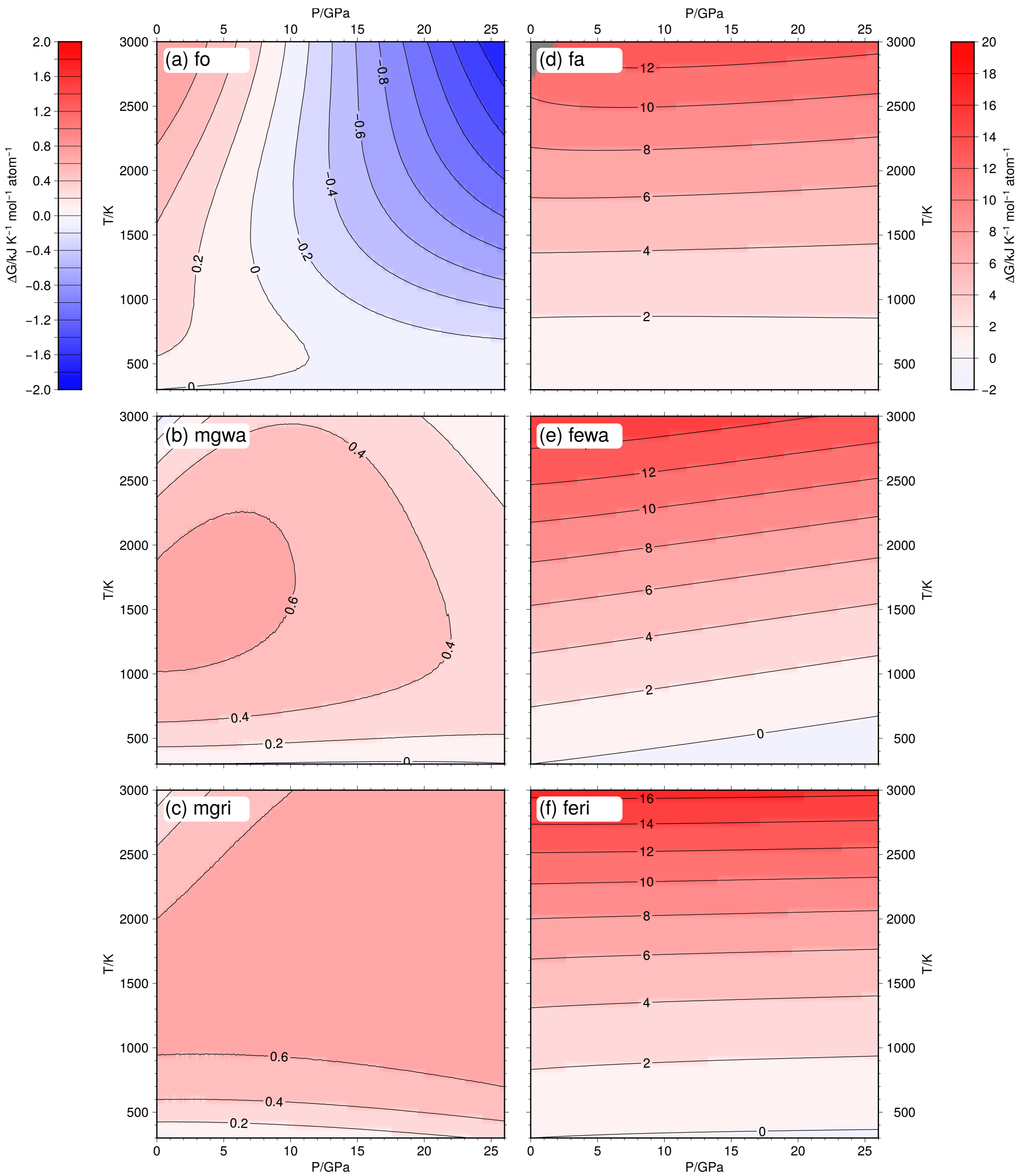

Figure S4: Differences of Gibbs energies computed using the parameter set of *Stixrude and Lithgow-Bertelloni* [2011] relative to those computed using parameters from *Holland et al.* [2013] as a function of P and T. Differences have been normalized to zero at ambient pressure and temperature. Panels (a), (b) and (c) show results for the Mg_2SiO_4 polymorphs forsterite, Mg-wadsleyite and Mg-ringwoodite. Panels (d), (e) and (f) show results for the Fe_2SiO_4 polymorphs fayalite, Fe-wadsleyite and ahrensite (Fe-ringwoodite).

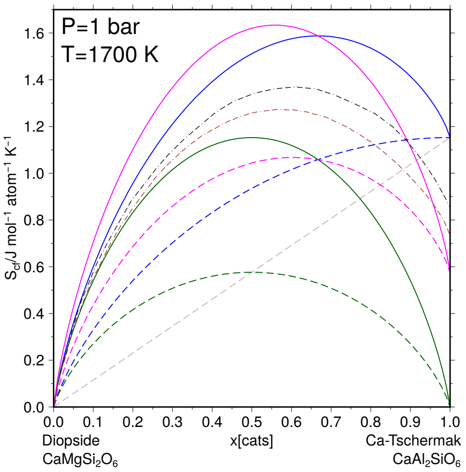

Figure S5: Entropy of solution between diopside ($CaMgSi_2O_6$) and Ca-tschermak ($CaAl_2SiO_6$): the solid blue, green and magenta lines represent mixing entropies for ionic models with two or three effective mixing sites, the dashed colored lines represent charge-coupled models with one or two effective mixing sites. The dashed gray line represents a linear combination of endmember entropies with internal disorder. The solid blue and dashed gray entropy curves are computed using the structure (Ca)(Mg)(Si)$_2$O$_6$ for clinodiopside and (Ca)(Al)(Al$_{\frac{1}{2}}$Si$_{\frac{1}{2}}$)$_2$O$_6$ for Ca-tschermak, while the solid green curve results from a structure (Ca)(Mg)(Si)SiO$_6$ for clinodiopside and (Ca)(Al)(Al)SiO$_6$ for Ca-tschermak. The solid magenta curve is computed using the structure (Ca)(Mg)(Si)(Si)O$_6$ for clinodiopside and (Ca)(Al)(Al$_{\frac{1}{2}}$Si$_{\frac{1}{2}}$)((Al$_{\frac{1}{2}}$Si$_{\frac{1}{2}}$))O$_6$ for Ca-tschermak. The dashed colored curves use structures analogous to those for the solid curves, but omitting the Mg-Al mixing terms. The two dash-dotted curves represent configuration entropy models by *Vinograd* [2001] (brown) and *Cohen* [1986] (black).

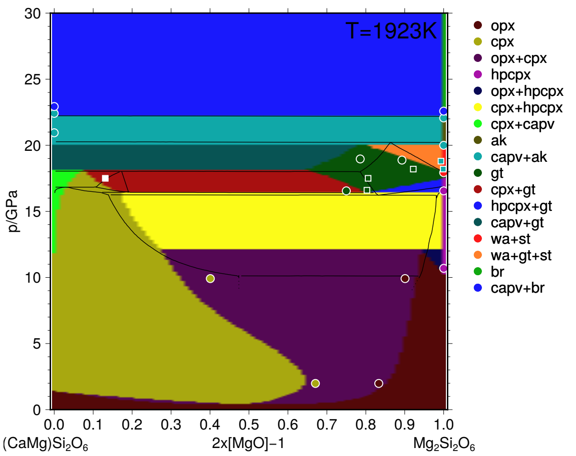

Figure S6: Stable phases along the diopside-enstatite (($(CaMg)Si_2O_6$)-$Mg_2Si_2O_6$) join at T=1923 K computed using MMA-EoS using the thermodynamic parameters from *Stixrude and Lithgow-Bertelloni* [2011] with 0.1 GPa and 1 mol% grid spacing. The phase stability fields are color-coded according to the legend (for abbreviations see Table S1). Circles show experimental data for the assemblage in matching colors, compiled in *Stixrude and Lithgow-Bertelloni* [2011]. Squares show experimental data from *Gasparik* [1990a], the white square indicates the CM phase. Solid lines are phase boundaries reported in *Gasparik* [2003], dotted lines are extrapolated from that assessment.

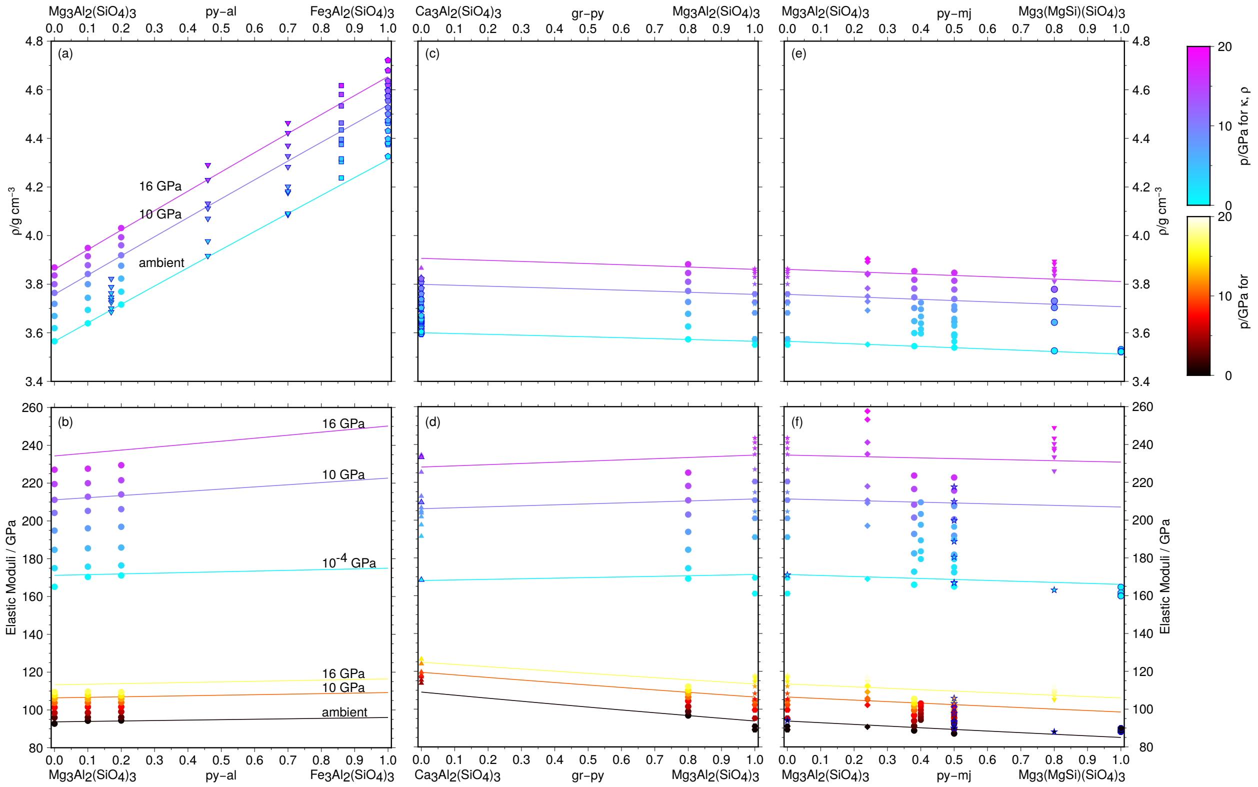

Figure S7: Compositional dependence of elastic properties in garnet binary solutions computed with MMA-EoS using model parameters from *Stixrude and Lithgow-Bertelloni* [2011] at room T. Panels (a) and (b) contain properties along the pyrope-almandine join; panels (c) and (d) for the grossular-pyrope join; panels (e) and (f) for the pyrope-Mg-majorite join. Panels (a), (c) and (e) show densities, panels (b), (d) and (f) elastic moduli. The properties have been computed at three different pressures (1 bar, 10 GPa, 16 GPa) and both experimental data and computed curves are color-coded by pressure (blue to magenta colors are used for the bulk moduli and densities, dark red to light yellow colors for the shear moduli). Experimental data are shown with symbols. In the pyrope-almandine system (a) and (b): *Chantel* [2012] (circles), *Huang and Chen* [2014] (inverse triangles with outline), *Fan et al.* [2009] (squares with outline), and *Zhang et al.* [1999] (pentagons with outline). In the grossular-pyrope system (c and d): *Kono et al.* [2010] (triangles), *Gréaux et al.* [2011] (triangles with outline), *Zhang et al.* [1999] (pentagons with outline), *Pavese et al.* [2001] (hexagons with outline), *Gwanmesia et al.* [2006] (hexagons), *Chantel* [2012] (circles), and *Zou et al.* [2012] (stars). In the pyrope-Mg-majorite system (e and f): *Gwanmesia et al.* [2006] (hexagons), *Zou et al.* [2012] (stars), *Sinogeikin and Bass* [2002a, b] (stars with outline), *Pamato et al.* [2016] (diamonds), *Chantel* [2012] (circles), *Gwanmesia et al.* [2009] (octagons), *Liu et al.* [2015] (inverse triangles), *Morishima et al.* [1999] (circles with outline), and *Gwanmesia et al.* [1998] (octagons with outline). To avoid confusion, data from *Chantel* [2012] for pure pyrope are only shown in panels (a and b).

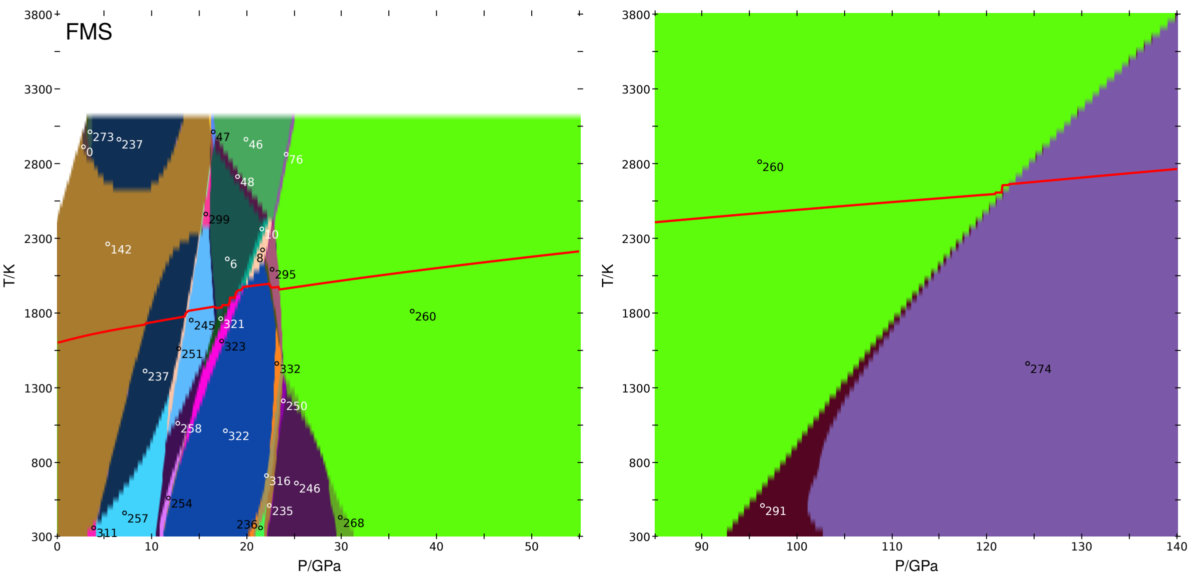

Figure S8: Phase diagrams computed with MMA-EoS using model parameters from *Stixrude and Lithgow-Bertelloni* [2011] for FMS composition (Table 2) as a function of P and T with 0.1 GPa and 50 K grid spacing. The left panel shows the P-range $0 - 55$ GPa (surface to lower mantle), the right panel shows the P-range $85 - 140$ GPa (lowermost mantle). An isentrope computed with predicted material properties, starting with 1600 K at 0 GPa is shown on top of the phase diagrams as a red line. Numbered stability fields (Table S2; for abbreviations, see Table S1) contain the following phase assemblages for the low-P region (left panel): (0) ol+opx+cpx, (6) wa+gt, (8) ri+gt, (10) wa+ri+gt, (46) gt+fp, (47) ol+gt+fp, (48) wa+gt+fp, (76) gt+br+fp, (142) ol+opx, (235) ak+fp, (236) ri+ak+fp, (237) ol+hpcpx, (245) wa+hpcpx, (246) st+fp, (251) ol+wa+hpcpx, (254) ri+hpcpx, (257) ol+ri+hpcpx, (258) wa+ri+hpcpx, (260) br+fp, (268) st+br+fp, (273) ol+cpx+hpcpx, (295) ri+br, (299) wa+opx, (311) ol+ri+opx, (316) ri+ak, (321) wa+st, (322) ri+st, (323) wa+ri+st, (332) ri+ak+st. Important phase transitions for the Mg_2SiO_4-based minerals along the isentrope are ol $\rightarrow$ wa (237 $\rightarrow$ 245 at 13.4 GPa and 1780 K), wa $\rightarrow$ ri (6 $\rightarrow$ (10) $\rightarrow$ 322 at 19.1 GPa and 1930 K), ri $\rightarrow$ br+pc (322 $\rightarrow$ (295) $\rightarrow$ 260 at 23.5 GPa and 1940 K). Phase fields given in parentheses indicate coexistence regions; in those cases, P and T refer to conditions at the center of the intersection between isentrope and coexistence region. In the $MgSiO_3$-based system, relevant phase transitions along the isentrope are opx $\rightarrow$ hpcpx (142 $\rightarrow$ 237 at 9.4 GPa and 1710 K), and hpcpx $\rightarrow$ wa + st (245 $\rightarrow$ 321 at 17.9 GPa and 1840 K). In the high-P region (right panel) the following phase assemblages occur: (260) br+fp, (274) ppv+fp, (291) br+ppv+fp. The isentrope crosses the br $\rightarrow$ ppv phase boundary (260 $\rightarrow$ 274) at 122.3 GPa and 2650 K.

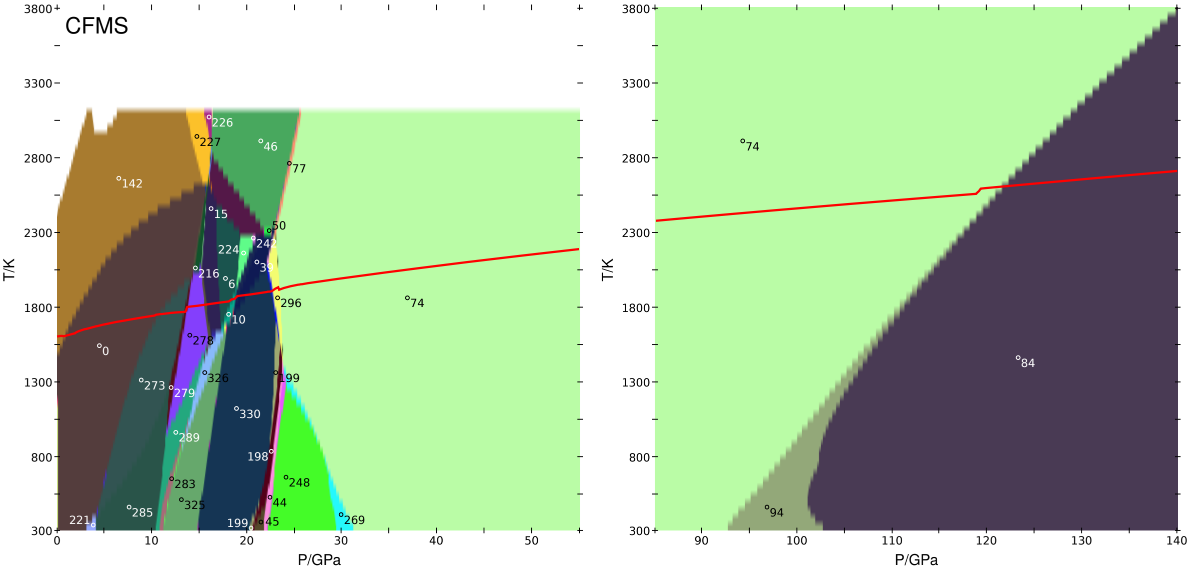

Figure S9: Phase diagrams computed with MMA-EoS using the parameters from *Stixrude and Lithgow-Bertelloni* [2011] for CFMS composition (Table 2) as a function of P and T with 0.1 GPa and 50 K grid spacing. The left panel shows the P-range $0-55$ GPa (surface to lower mantle), the right panel shows the P-range $85-140$ GPa (lowermost mantle). An isentrope computed with predicted material properties for the CFMAS system (Figure S10), starting with 1600 K at 0 GPa is shown on top of the phase diagrams as a red line. Numbered stability fields (Table S2; for abbreviations, see Table S1) contain the following phase assemblages for the low-P region (left panel): (0) ol+opx+cpx, (6) wa+gt, (10) wa+ri+gt, (15) wa+cpx+gt, (39) ri+capv+gt, (44) capv+ak+fp, (45) ri+capv+ak+fp, (46) gt+fp, (50) ri+gt+fp, (74) capv+br+fp, (77) capv+gt+br+fp, (142) ol+opx, (198) ri+capv+ak, (199) ri+capv+ak+st, (216) wa+opx+cpx, (221) ol+ri+opx+cpx, (224) wa+capv+gt, (226) opx+fp, (227) ol+opx+fp, (242) wa+capv+gt+fp, (248) capv+st+fp, (269) capv+st+br+fp, (273) ol+cpx+hpcpx, (278) wa+cpx+hpcpx, (279) ol+wa+cpx+hpcpx, (283) ri+cpx+hpcpx, (285) ol+ri+cpx+hpcpx, (289) wa+ri+cpx+hpcpx, (296) ri+capv+br, (325) ri+cpx+st, (326) wa+ri+cpx+st, (330) ri+capv+st. Along the isentrope the following transitions occur in the Mg_2SiO_4-based system: ol $\rightarrow$ wa (273 $\rightarrow$ (279) $\rightarrow$ 278 at 13.6 GPa and 1770 K), wa $\rightarrow$ ri (6 $\rightarrow$ (10) $\rightarrow$ 39 at 18.5 GPa and 1840 K), ri+st $\rightarrow$ br+fp (330 $\rightarrow$ (296) $\rightarrow$ 74 at 22.9 GPa and 1920 K). In the $MgSiO_3$-based system the following transitions occur: opx $\rightarrow$ cpx+hpcpx (142 $\rightarrow$ (0) $\rightarrow$ 273 between 1.0 GPa and 10.5 GPa, 1600 K and 1730 K), hpcpx $\rightarrow$ gt (278 $\rightarrow$ 15 at 15.6 GPa and 1790 K), cpx $\rightarrow$ gt (15 $\rightarrow$ 6 at 17.0 GPa and 1820 K), gt $\rightarrow$ capv+st (10 $\rightarrow$ (39) $\rightarrow$ 330 between 18.7 GPa and 19.9 GPa, 1860 K and 1870 K). In the high-P region (right panel) the following phase assemblages occur: (74) capv+br+fp, (84) capv+ppv+fp, (94) capv+br+ppv+fp. The isentrope intersects the br $\rightarrow$ ppv phase boundary (74 $\rightarrow$ 84) at 121.8 GPa and 2610 K. Phase fields given in parentheses indicate coexistence regions; in those cases, P and T refer to conditions at the boundaries or the center of the intersection between isentrope and coexistence region.

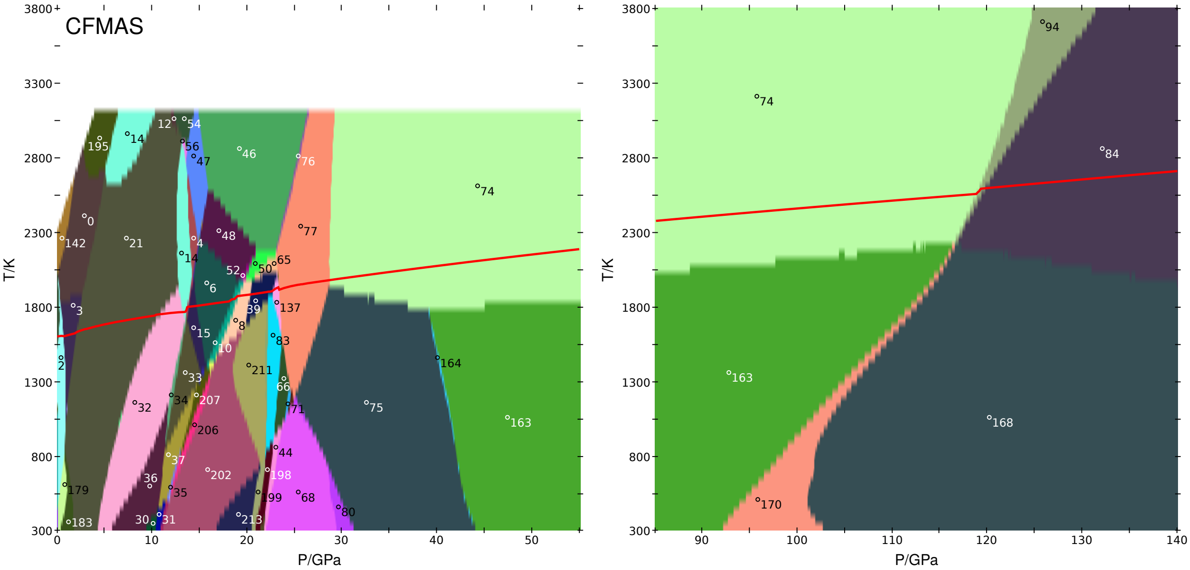

Figure S10: Phase diagrams computed with MMA-EoS using the parameters from *Stixrude and Lithgow-Bertelloni* [2011] for CFMAS composition (Table 2) as a function of P and T with 0.1 GPa and 50 K grid spacing. The left panel shows the P-range 0 − 55 GPa (surface to lower mantle), the right panel shows the P-range 85 − 140 GPa (lowermost mantle). An isentrope computed with predicted material properties, starting with 1600 K at 0 GPa is shown on top of the phase diagrams as a red line. Numbered stability fields (Table S2; for abbreviations, see Table S1) contain the following phase assemblages for the low-P region (left panel): (0) ol+opx+cpx, (2) fsp+ol+opx+cpx, (3) sp+ol+opx+cpx, (4) ol+gt, (6) wa+gt, (8) ri+gt, (10) wa+ri+gt, (12) ol+opx+gt, (14) ol+cpx+gt, (15) wa+cpx+gt, (21) ol+opx+cpx+gt, (30) ol+ri+hpcpx+gt, (31) wa+ri+hpcpx+gt, (32) ol+cpx+hpcpx+gt, (33) wa+cpx+hpcpx+gt, (34) ol+wa+cpx+hpcpx+gt, (35) ri+cpx+hpcpx+gt, (36) ol+ri+cpx+hpcpx+gt, (37) wa+ri+cpx+hpcpx+gt, (39) ri+capv+gt, (44) capv+ak+fp, (46) gt+fp, (47) ol+gt+fp, (48) wa+gt+fp, (50) ri+gt+fp, (52) wa+ri+gt+fp, (54) ol+opx+gt+fp, (56) ol+cpx+gt+fp, (65) ri+capv+gt+fp, (66) capv+ak+gt+fp, (68) capv+ak+st+fp, (71) capv+ak+gt+st+fp, (74) capv+br+fp, (75) capv+ak+br+fp, (76) gt+br+fp, (77) capv+gt+br+fp, (80) capv+ak+st+br+fp, (83) ri+capv+ak+gr+fp, (137) ri+capv+gt+br, (142) ol+opx, (163) capv+br+fp+cf, (164) capv+ak+br+fp+cf, (179) ol+opx+cpx+ky, (183) ol+opx+cpx+gt+ky, (195) ol+cpx, (198) ri+capv+ak, (199) ri+capv+ak+st, (202) ri+gt+st, (206) ri+cpx+gt+st, (207) wa+ri+cpx+gt+st, (211) ri+capv+gt+st, (213) ri+ak+gt+st Along the isentrope the following transitions occur in the Mg_2SiO_4-based system: ol → wa (14 → 15 at 13.7 GPa and 1770 K), wa → ri (6 → (10) → 8 at 18.7 GPa and 1850 K), ri → br+fp (137 → 77 at 23.4 GPa and 1930 K). In the $MgSiO_3$-based system the following transitions occur: fsp → sp (2 → 3 at 0.7 GPa and 1600 K), sp → gt (3 → 21 at 1.9 GPa and 1630 K), opx+cpx → cpx+hpcpx+gt (3 → (21) → 32 between 1.9 GPa and 10.7 GPa, 1630 K and 1740 K), hpcpx → gt (32 → 14 at 13.2 GPa and 1750 K), cpx → gt (15 → 6 at 14.7 GPa and 1800 K), gt → capv+br (8 → (39, 137, 77) → 74 between 20.4 GPa and 28.7 GPa, 1890 K and 1980 K) via capv in (8 → 39 at 20.3 GPa and 1880 K), br in (39 → 137 at 22.6 GPa and 1900 K) and gt out (77 → 74 at 28.7 GPa and 1970 K). In the high-P region (right panel) the following phase assemblages occur: (74) capv+br+fp, (84) capv+ppv+fp, (94) capv+br+ppv+fp, (163) capv+br+fp+cf, (168) capv+ppv+fp+cf, (170) capv+br+ppv+fp+cf. The isentrope intersects the br → ppv phase boundary (74 → (94) → 84 at 119.1 GPa and 2570 K). Phase fields given in parentheses indicate coexistence regions; in those cases, P and T refer to conditions at the boundaries or the center of the intersection between isentrope and coexistence region.

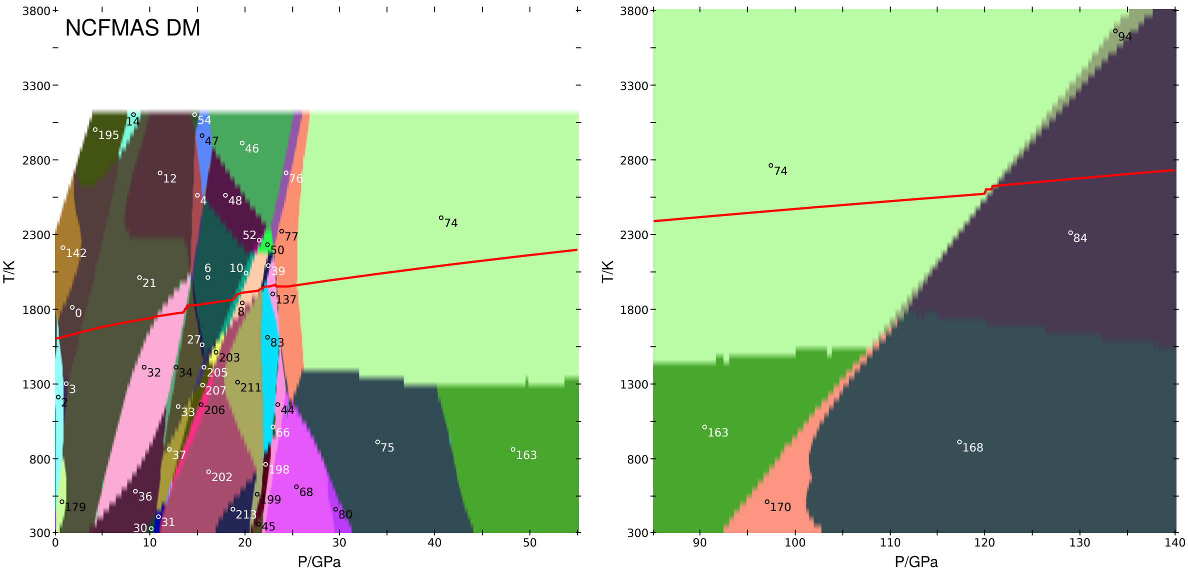

Figure S11: Phase diagrams computed with MMA-EoS using the model parameters from *Stixrude and Lithgow-Bertelloni* [2011] for depleted mantle (Table 2) as a function of P and T with 0.1 GPa and 50 K grid spacing. The left panel shows the P-range 0 − 55 GPa (surface to lower mantle), the right panel shows the P-range 85 − 140 GPa (lowermost mantle). An isentrope computed with predicted material properties, starting with 1600 K at 0 GPa is shown on top of the phase diagrams as a red line. Numbered stability fields (Table S2; for abbreviations, see Table S1) contain the following phase assemblages for the low-P region (left panel): (0) ol+opx+cpx, (2) fsp+ol+opx+cpx, (3) sp+ol+opx+cpx, (4) ol+gt, (6) wa+gt, (8) ri+gt, (10) wa+ri+gt, (12) ol+opx+gt, (14) ol+cpx+gt, (21) ol+opx+cpx+gt, (27) wa+hpcpx+gt, (30) ol+ri+hpcpx+gt, (31) wa+ri+hpcpx+gt, (32) ol+cpx+hpcpx+gt, (33) wa+cpx+hpcpx+gt, (34) ol+wa+cpx+hpcpx+gt, (36) ol+ri+cpx+hpcpx+gt, (37) wa+ri+cpx+hpcpx+gt, (39) ri+capv+gt, (44) capv+ak+fp, (45) ri+capv+ak+fp, (46) gt+fp, (47) ol+gt+fp, (48) wa+gt+fp, (50) ri+gt+fp, (52) wa+ri+gt+fp, (54) ol+opx+gt+fp, (68) capv+ak+st+fp, (74) capv+br+fp, (75) capv+ak+br+fp, (76) gt+br+fp, (77) capv+gt+br+fp, (80) capv+ak+st+br+fp, (83) ri+capv+ak+gt, (137) ri+capv+gt+br, (142) ol+opx, (179) ol+opx+cpx+ky, (195) ol+cpx, (198) ri+capv+ak, (199) ri+capv+ak+st, (202) ri+gt+st, (203) wa+ri+gt+st, (205) wa+cpx+gt+st, (206) ri+cpx+gt+st, (207) wa+ri+cpx+gt+st, (211) ri+capv+gt+st, (213) ri+ak+gt+st. Along the isentrope the following transitions occur in the Mg_2SiO_4-based system: ol → wa (32 → (34) → 33 at 13.7 GPa and 1800 K), wa → ri (6 → (10) → 8 at 18.8 GPa and 1870 K), ri → br+fp (137 → 77 at 23.3 GPa and 1950 K). In the $MgSiO_3$-based system the following transitions occur: fsp → opx+cpx (2 → 0 at 0.6 GPa and 1590 K), opx+cpx → cpx+hpcpx+gt (0 → (21) → 32 between 2.7 GPa and 10.7 GPa, 1630 K and 1740 K), cpx → hpcpx (33 → 27 at 14.6 GPa and 1820 K), hpcpx → gt (27 → 6 at 15.0 GPa and 1830 K), gt → capv+br+fp (8 → (39, 83, 137, 77) → 74 between 21.7 GPa and 25.4 GPa, 1930 K and 1960 K) via capv in (8 → 39 at 21.7 GPa and 1940 K), ak in (39 → 83 at 22.0 GPa and 1950 K), ak → br (83 → 137 at 22.5 GPa and 1950 K) and gt out (77 → 74 at 25.4 GPa and 1960 K). In the high-P region (right panel) the following phase assemblages occur: (74) capv+br+fp, (84) capv+ppv+fp, (94) capv+br+ppv+fp, (163) capv+br+fp+cf, (168) capv+ppv+fp+cf, (170) capv+br+ppv+fp+cf. The isentrope intersects the br → ppv phase boundary (74 → 84) at 120.8 GPa and 2600 K. Phase fields given in parentheses indicate coexistence regions; in those cases, P and T refer to conditions at the boundaries or the center of the intersection between isentrope and coexistence region.

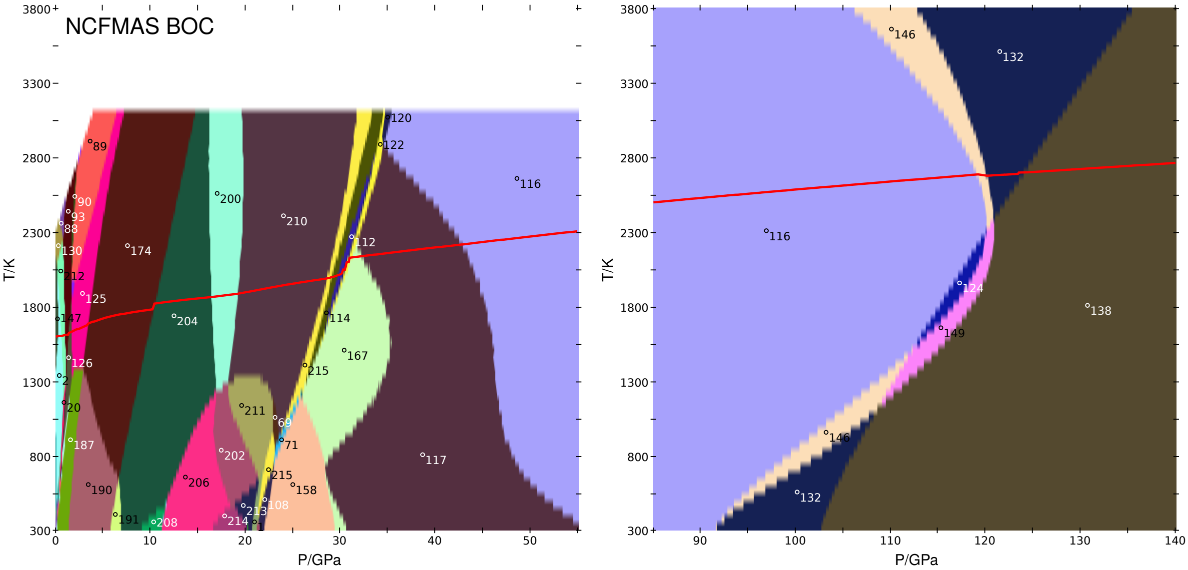

Figure S12: Phase diagrams computed with MMA-EoS using the model parameters from *Stixrude and Lithgow-Bertelloni* [2011] for bulk oceanic crust (Table 2) as a function of P and T with 0.1 GPa and 50 K grid spacing. The left panel shows the P-range $0 - 55$ GPa (surface to lower mantle), the right panel shows the P-range $85 - 140$ GPa (lowermost mantle). An isentrope computed with predicted material properties, starting with 1600 K at 0 GPa is shown on top of the phase diagrams as a red line. Numbered stability fields (Table S2; for abbreviations, see Table S1) contain the following phase assemblages for the low-P region (left panel): (1) ol+opx+cpx, (2) fsp+ol+opx+cpx, (20) fsp+opx+cpx+gt, (69) capv+gt+st+fp, (71) capv+ak+gt+st+fp, (88) fsp+opx+qz, (89) cpx+qz, (90) fsp+cpx+qz, (93) fsp+opx+cpx+qz, (108) capv+ak+st+cf, (112) capv+gt+st+cf, (114) capv+ak+gt+st+cf, (116) capv+st+br+cf, (117) capv+ak+st+br+cf, (120) capv+gt+st+br+cf, (122) capv+ak+gt+st+br+cf, (125) cpx+gt+qz, (126) fsp+cpx+gt+qz, (130) fsp+opx, (147) fsp+ol+opx, (158) capv+ak+st+fp+cf, (167) capv+ak+st+br+fp+cf, (174) cpx+gt+coes, (187) cpx+gt+qz+ky, (190) cpx+gt+coes+ky, (191) cpx+gt+st+ky, (200) gt+st, (202) ri+gt+st, (204) cpx+gt+st, (206) ri+cpx+gt+st, (208) cpx+hpcpx+gt+st, (210) capv+gt+st, (211) ri+capv+gt+st, (212) fsp+opx+cpx, (213) ri+ak+gt+st, (214) ri+cpx+ak+gt+st, (215) capv+ak+gt+st. Along the isentrope the following transitions occur in the $MgSiO_3$-based system: opx → cpx (93 → 126 at 1.2 GPa and 1610 K), fsp → cpx+gt (126 → 125 at 1.7 GPa and 1630 K), cpx → gt (204 → 200 at 16.4 GPa and 1860 K), gt → ak+capv+br+fp+cf (200 → (210, 215, 114, 112, 122) → 167 between 19.1 GPa and 31.2 GPa, 1880 K and 2120 K) via capv in (200 → 210 at 19.3 GPa and 1890 K), ak in (210 → 215 at 28.5 GPa and 1990 K), cafe in (215 → 114 at 29.1 GPa and 2000 K), ak out (114 → 112 at 29.8 GPa and 2010 K), br in (112 → 122 at 30.6 GPa and 2080 K) and gt out (122 → 167 at 31.1 GPa and 2130 K), ak+fp → br+cf (167 → (117) → 116 between 32.2 GPa and 42.7 GPa, 2130 K and 2210 K) via fp out (167 → 117 at 32.2 GPa and 2130 K) and ak out (117 → 116 at 42.7 GPa and 2210 K). The following SiO_2 phase transitions occur: qz → coes (125 → 174 at 3.3 GPa and 1680 K), coes → st (174 → 204 at 10.4 GPa and 1800 K). In the high-P region (right panel) the following phase assemblages occur: (116) capv+st+br+cf, (124) capv+sf+br+cf, (132) capv+st+ppv+cf, (138) capv+sf+ppv+cf, (146) capv+st+br+ppv+cf, (149) capv+sf+br+ppv+cf. The isentrope intersects the br → ppv phase boundary (116 → (146) → 132 between 119.0 GPa and 120.1 GPa, 2680 K and 2670 K) and the st → sf phase boundary (132 → 138 at 124.3 GPa and 2700 K). Phase fields given in parentheses indicate coexistence regions; in those cases P and T refer to conditions at the boundaries or the center of the intersection between isentrope and coexistence region.

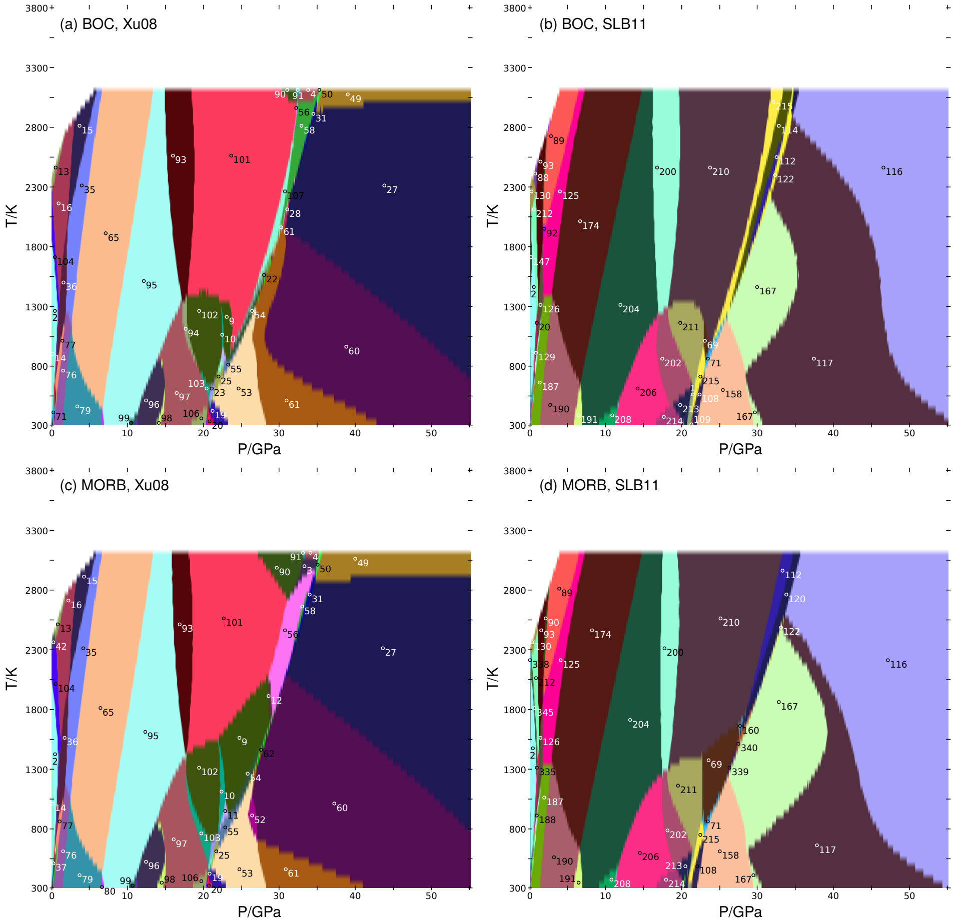

Figure S13: *P*-*T* phase diagrams computed for two basaltic compositions: BOC (Table 2) in the top row and a mid-ocean ridge basalt by *Presnall and Hoover* [1987], reduced to six components, as used by *Xu et al.* [2008] (lower row). Computations used 0.1 GPa and 50 K grid spacing. Phase relations have been calculated with the Mie-Grüneisen-Debye-Birch-Murnaghan model using the thermodynamic dataset of *Xu et al.* [2008] (left column) and *Stixrude and Lithgow-Bertelloni* [2011] (right column). The phase fields with the same numbers in the left and right columns represent different phase assemblages; consult Table S3 for the left column and Table S2 for the right column. In panels (a) and (c) the following phase assemblages occur: (2) fsp+ol+opx+cpx, (3) capv+gt+st+br+ppv, (4) capv+ak+gt+st+br+ppv, (9) capv+gt+st+fp, (10) ri+capv+gt+st+fp, (11) capv+ak+gt+st+fp, (12) capv+gt+st+br+fp , (13) fsp+opx+qz, (14) fsp+ol+cpx+qz, (15) opx+cpx+qz, (16) fsp+opx+cpx+qz, (19) capv+ak+st+cf, (20) ri+capv+ak+st+cf, (22) capv+gt+st+cf, (23) ri+capv+gt+st+cf, (25) capv+ak+gt+st+cf, (27) capv+st+br+cf, (28) capv+ak+st+br+cf, (31) capv+gt+st+br+cf, (35) cpx+gt+qz, (36) fsp+cpx+gt+qz, (37) fsp+ol+cpx+gt+qz, (42) fsp+opx, (49) capv+st+br+ppv+cf, (50) capv+gt+st+br+ppv+cf, (52) capv+st+fp+cf, (53) capv+ak+st+fp+cf, (54) capv+gt+st+fp+cf, (55) capv+ak+gt+st+fp+cf, (56) capv+gt+st+br, (58) capv+ak+gt+st+br, (60) capv+st+br+fp+cf, (61) capv+ak+st+br+fp+cf, (62) capv+gt+st+br+fp+cf, (65) cpx+gt+coes, (71) fsp+ol+cpx+gt+ky, (76) cpx+gt+qz+ky, (77) fsp+cpx+gt+qz+ky, (79) cpx+gt+coes+ky, (80) cpx+gt+st+ky, (90) capv+gt+st+ppv, (91) capv+ak+gt+st+ppv, (93) gt+st, (94) ri+gt+st, (95) cpx+gt+st, (96) wa+cpx+gt+st, (97) ri+cpx+gt+st, (98) wa+ri+cpx+gt+st, (99) cpx+hpcpx+gt+st, (101) capv+gt+st, (102) ri+capv+gt+st, (103) ri+cpx+capv+gt+st, (104) fsp+opx+cpx, (106) ri+cpx+ak+gt+st, (107) capv+ak+gt+st. In panels (b) and (d) the following phase assemblages are predicted: (2) fsp+ol+opx+cpx, (20) fsp+opx+cpx+gt, (69) capv+gt+st+fp, (71) capv+ak+gt+st+fp, (88) fsp+opx+qz, (89) cpx+qz, (90) fsp+cpx+qz, (92) opx+cpx+qz, (93) fsp+opx+cpx+qz, (108) capv+ak+st+cf, (109) ri+capv+ak+st+cf, (112) capv+gt+st+cf, (114) capv+ak+gt+st+cf, (116) capv+st+br+cf, (117) capv+ak+st+br+cf, (120) capv+gt+st+br+cf, (122) capv+ak+gt+st+br+cf, (125) cpx+gt+qz, (126) fsp+cpx+gt+qz, (129) fsp+opx+cpx+gt+qz, (130) fsp+opx, (147) fsp+ol+opx, (158) capv+ak+st+fp+cf, (160) capv+gt+st+br, (167) capv+ak+st+br+fp+cf, (174) cpx+gt+coes, (187) cpx+gt+qz+ky, (188) fsp+cpx+gt+qz+ky, (190) cpx+gt+coes+ky, (191) cpx+gt+st+ky, (200) gt+st, (202) ri+gt+st, (204) cpx+gt+st, (206) ri+cpx+gt+st, (208) cpx+hpcpx+gt+st, (210) capv+gt+st, (211) ri+capv+gt+st, (212) fsp+opx+cpx, (213) ri+ak+gt+st, (214) ri+cpx+ak+gt+st, (215) capv+ak+gt+st, (335) fsp+sp+opx+cpx+gt, (338) fsp+sp+opx, (339) capv+gt+st+fp+cf, (340) capv+gt+st+pv+fp+cf, (345) fsp+sp+opx+cpx.

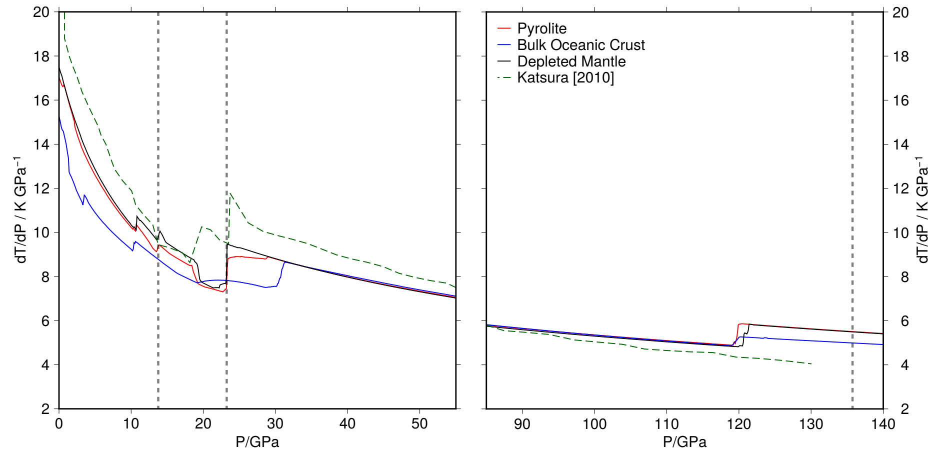

Figure S14: Pressure derivative of isentropes computed self-consistently using the model parameters from *Stixrude and Lithgow-Bertelloni* [2011] (solid red, blue and black lines). The adiabatic gradient from *Katsura et al.* [2010] is shown for comparison (dashed green line). See Figure 17 for the corresponding isentropes.

Table S1: Endmember and solution phases in the dataset of *Stixrude and Lithgow-Bertelloni* [2011]. Solution entropies are symmetric except for internal disorder of endmembers. The notation of the parentheses to identify mixing sites is introduced in Section S3.2. Virtual solution endmembers are listed in *italics*.

Phase	**Endmember**	**Formula**
Plagioclase feldspar (fsp)	Anorthite (an)	$(Ca)(Al_2Si_2)O_8$
	Albite (ab)	$(Na)(AlSi_3)O_8$
Spinel (sp)	Spinel (sp)	$(MgAl_7)(Mg_3Al)O_{16}$
	Hercynite (hc)	$(FeAl_7)(Fe_3Al)O_{16}$
Olivine (ol)	Forsterite (fo)	$(Mg_2)SiO_4$
	Fayalite (fa)	$(Fe_2)SiO_4$
Wadsleyite (wa)	Mg-Wadsleyite (mgwa)	$(Mg_2)SiO_4$
	Fe-Wadsleyite (fewa)	$(Fe_2)SiO_4$
Ringwoodite (ri)	Mg-Ringwoodite (mgri)	$(Fe_2)SiO_4$
	Ahrensite (feri)	$(Fe_2)SiO_4$
Orthopyroxene (opx)	Enstatite (en)	$(Mg)(Mg)Si_2O_6$
	Ferrosilite (fs)	$(Fe)(Fe)Si_2O_6$
	Mg-Tschermak (mgts)	$(Mg)(Al)SiAlO_6$
	Ortho-Diopside (odi)	$(Ca)(Mg)Si_2O_6$
Clinopyroxene (cpx)	Diopside (di)	$(Ca)(Mg)(Si_2)O_6$
	Hedenbergite (he)	$(Ca)(Fe)(Si_2)O_6$
	Clinoenstatite (cen)	$(Mg)(Mg)(Si_2)O_6$
	Ca-Tschermak (cats)	$(Ca)(Al)(SiAl)O_6$
	Jadeite (jd)	$(Na)(Al)(Si_2)O_6$
HP-Clinopyroxene (hpcpx)	HP-Clinoenstatite (hpcen)	$(Mg_2)Si_2O_6$
	HP-Clinoferrosilite (hpcfs)	$(Fe_2)Si_2O_6$
Ca-Perovskite (capv)		$CaSiO_3$
Akimotoite (ak)	Mg-Akimotoite (mgak)	$(Mg)(Si)O_3$
	Hemleyite (feak)	$(Fe)(Si)O_3$
	Corundum (co)	$(Al)(Al)O_3$
Garnet (gt)	Pyrope (py)	$(Mg_3)(Al)(Al)Si_3O_{12}$
	Almandine (al)	$(Fe_3)(Al)(Al)Si_3O_{12}$
	Grossular (gr)	$(Ca_3)(Al)(Al)Si_3O_{12}$
	Mg-Majorite (mj)	$(Mg_3)(Mg)(Si)Si_3O_{12}$
	Jadeite-Majorite (jdmj)	$(Na_2Al)(Al)(Si)Si_3O_{12}$
Quartz (qz)		SiO_2
Coesite (coes)		SiO_2
Stishovite (st)		SiO_2
Seifertite (sf)		SiO_2
Bridgmanite (br)	Mg-Bridgmanite (mgbr)	$(Mg)(Si)O_3$
	Fe-Bridgmanite (febr)	$(Fe)(Si)O_3$
	Al-Bridgmanite (albr)	$(Al)(Al)O_3$
Post-Perovskite (ppv)	*Mg-Post-Perovskite* (mppv)	$(Mg)(Si)O_3$
	Fe-Post-Perovskite (fppv)	$(Fe)(Si)O_3$
	Al-Post-Perovskite (appv)	$(Al)(Al)O_3$
Ferropericlase (fp)	Periclase (pe)	$(Mg)O$
	Wüstite (wu)	$(Fe)O$
Ca-Ferrite (cf)	*Mg-Ca-Ferrite* (mgcf)	$(Mg)(Al)AlO_4$
	Fe-Ca-Ferrite (fecf)	$(Fe)(Al)AlO_4$
	Na-Ca-Ferrite (nacf)	$(Na)(Si)AlO_4$
Kyanite (ky)		Al_2SiO_5
Nepheline (neph)		$NaAlSiO_4$

Id	Phases in Stable Assemblage
0	ol, opx, cpx
1	ri, capv, ak, gt, st
2	fsp, ol, opx, cpx
3	sp, ol, opx, cpx
4	ol, gt
6	wa, gt
7	ol, wa, gt
8	ri, gt
9	sp, ri, gt
10	wa, ri, gt
12	ol, opx, gt
14	ol, cpx, gt
15	wa, cpx, gt
16	ol, wa, cpx, gt
20	fsp, opx, cpx, gt
21	ol, opx, cpx, gt
26	ol, hpcpx, gt
27	wa, hpcpx, gt
28	ri, hpcpx, gt
30	ol, ri, hpcpx, gt
31	wa, ri, hpcpx, gt
32	ol, cpx, hpcpx, gt
33	wa, cpx, hpcpx, gt
34	ol, wa, cpx, hpcpx, gt
35	ri, cpx, hpcpx, gt
36	ol, ri, cpx, hpcpx, gt
37	wa, ri, cpx, hpcpx, gt
39	ri, capv, gt
44	capv, ak, fp
45	ri, capv, ak, fp
46	gt, fp
47	ol, gt, fp
48	wa, gt, fp
49	ol, wa, gt, fp
50	ri, gt, fp
52	wa, ri, gt, fp
54	ol, opx, gt, fp
56	ol, cpx, gt, fp
65	ri, capv, gt, fp
66	capv, ak, gt, fp
67	ri, capv, ak, gt, fp
68	capv, ak, st, fp
69	capv, gt, st, fp
71	capv, ak, gt, st, fp
72	ri, ak, gt
74	capv, br, fp
75	capv, ak, br, fp
...	*continued in next column*

Id	Phases in Stable Assemblage
76	gt, br, fp
77	capv, gt, br, fp
79	capv, ak, gt, br, fp
80	capv, ak, st, br, fp
83	ri, capv, ak, gt
84	capv, ppv, fp
85	gt, ppv, fp
88	fsp, opx, qz
89	cpx, qz
90	fsp, cpx, qz
92	opx, cpx, qz
93	fsp, opx, cpx, qz
94	capv, br, ppv, fp
97	ri, capv, ak, cf
108	capv, ak, st, cf
109	ri, capv, ak, st, cf
112	capv, gt, st, cf
114	capv, ak, gt, st, cf
116	capv, st, br, cf
117	capv, ak, st, br, cf
120	capv, gt, st, br, cf
122	capv, ak, gt, st, br, cf
124	capv, sf, br, cf
125	cpx, gt, qz
126	fsp, cpx, gt, qz
129	fsp, opx, cpx, gt, qz
130	fsp, opx
132	capv, st, ppv, cf
133	ri, gt, br
137	ri, capv, gt, br
138	capv, sf, ppv, cf
142	ol, opx
146	capv, st, br, ppv, cf
147	fsp, ol, opx
149	capv, sf, br, ppv, cf
156	capv, ak, fp, cf
157	ri, capv, ak, fp, cf
158	capv, ak, st, fp, cf
160	capv, gt, st, br
163	capv, br, fp, cf
164	capv, ak, br, fp, cf
165	capv, gt, br, fp, cf
167	capv, ak, st, br, fp, cf
168	capv, ppv, fp, cf
170	capv, br, ppv, fp, cf
174	cpx, gt, coes
179	ol, opx, cpx, ky
...	*continued in next column*

Id	Phases in Stable Assemblage
183	ol, opx, cpx, gt, ky
187	cpx, gt, qz, ky
188	fsp, cpx, gt, qz, ky
190	cpx, gt, coes, ky
191	cpx, gt, st, ky
195	ol, cpx
198	ri, capv, ak
199	ri, capv, ak, st
200	gt, st
201	wa, gt, st
202	ri, gt, st
203	wa, ri, gt, st
204	cpx, gt, st
205	wa, cpx, gt, st
206	ri, cpx, gt, st
207	wa, ri, cpx, gt, st
208	cpx, hpcpx, gt, st
210	capv, gt, st
211	ri, capv, gt, st
212	fsp, opx, cpx
213	ri, ak, gt, st
214	ri, cpx, ak, gt, st
215	capv, ak, gt, st
216	wa, opx, cpx
219	ol, wa, opx, cpx
221	ol, ri, opx, cpx
222	ol, wa, hpcpx, gt
224	wa, capv, gt
226	opx, fp
227	ol, opx, fp
235	ak, fp
236	ri, ak, fp
237	ol, hpcpx
238	sp, gt, fp
239	wa, cpx, gt, fp
242	wa, capv, gt, fp
243	ak, gt, fp
245	wa, hpcpx
246	st, fp
248	capv, st, fp
250	ak, st, fp
251	ol, wa, hpcpx
254	ri, hpcpx
257	ol, ri, hpcpx
258	wa, ri, hpcpx
260	br, fp
263	ri, sf
...	*continued in next column*

Id	Phases in Stable Assemblage
265	ak, br, fp
268	st, br, fp
269	capv, st, br, fp
270	ak, st, br, fp
273	ol, cpx, hpcpx
274	ppv, fp
278	wa, cpx, hpcpx
279	ol, wa, cpx, hpcpx
280	ol, qz
283	ri, cpx, hpcpx
285	ol, ri, cpx, hpcpx
286	sf, ppv, fp
289	wa, ri, cpx, hpcpx
291	br, ppv, fp
294	wa, br
295	ri, br
296	ri, capv, br
298	sp, ol, opx
299	wa, opx
300	ri, st, br
302	ri, capv, st, br
303	br, fp, cf
304	ak, br, fp, cf
306	ppv, fp, cf
307	br, ppv, fp, cf
311	ol, ri, opx
312	wa, ak
313	ol, opx, ky
314	ol, opx, gt, ky
316	ri, ak
317	ol, opx, ak
321	wa, st
322	ri, st
323	wa, ri, st
325	ri, cpx, st
326	wa, ri, cpx, st
329	ri, cpx, hpcpx, st
330	ri, capv, st
332	ri, ak, st
335	fsp, sp, opx, cpx, gt
338	fsp, sp, opx
339	capv, gt, st, fp, cf
340	capv, gt, st, pv, fp, cf
345	fsp, sp, opx, cpx

Table S2: Numbering of stable phase assemblages in phase diagrams for (reduced) pyrolite compositions (Figures 9, S8, S9, 10, S10 and 11),depleted mantle (Figure S11) and bulk oceanic crust (Figure S12), and the right panels of Figure S13). Phase abbreviations are listed in Table S1. Gaps in numbering correspond to phase assemblages that do not occur at a significant number of grid points.

Id	Phases in Stable Assemblage
2	fsp, ol, opx, cpx
3	capv, gt, st, br, ppv
4	capv, ak, gt, st, br, ppv
9	capv, gt, st, fp
10	ri, capv, gt, st, fp
11	capv, ak, gt, st, fp
12	capv, gt, st, br, fp
13	fsp, opx, qz
14	fsp, ol, cpx, qz
15	opx, cpx, qz
16	fsp, opx, cpx, qz
19	capv, ak, st, cf
20	ri, capv, ak, st, cf
22	capv, gt, st, cf
23	ri, capv, gt, st, cf
25	capv, ak, gt, st, cf
27	capv, st, br, cf
28	capv, ak, st, br, cf
31	capv, gt, st, br, cf
35	cpx, gt, qz
36	fsp, cpx, gt, qz
37	fsp, ol, cpx, gt, qz
42	fsp, opx
49	capv, st, br, ppv, cf
50	capv, gt, st, br, ppv, cf
52	capv, st, fp, cf
53	capv, ak, st, fp, cf
54	capv, gt, st, fp, cf
55	capv, ak, gt, st, fp, cf
56	capv, gt, st, br
58	capv, ak, gt, st, br
60	capv, st, br, fp, cf
61	capv, ak, st, br, fp, cf
62	capv, gt, st, br, fp, cf
65	cpx, gt, coes
71	fsp, ol, cpx, gt, ky
76	cpx, gt, qz, ky
77	fsp, cpx, gt, qz, ky
79	cpx, gt, coes, ky
80	cpx, gt, st, ky
90	capv, gt, st, ppv
91	capv, ak, gt, st, ppv
93	gt, st
94	ri, gt, st
95	cpx, gt, st
96	wa, cpx, gt, st
97	ri, cpx, gt, st
...	*continued in next column*
98	wa, ri, cpx, gt, st
99	cpx, hpcpx, gt, st
101	capv, gt, st
102	ri, capv, gt, st
103	ri, cpx, capv, gt, st
104	fsp, opx, cpx
106	ri, cpx, ak, gt, st
107	capv, ak, gt, st

Table S3: Numbering of stable phase assemblages in computed phase diagrams for bulk oceanic crust and mid-ocean ridge basalt compositions using the thermodynamic dataset of *Xu et al.* [2008], used in the left panels of Figure S13. Phase abbreviations are listed in Table S1. Gaps in numbering correspond to phase assemblages that do not occur at a significant number of grid points.